Biochemistry **2007,** *46,* 7233−7251

Effects of Surface Adsorption on Catalytic Activity of Heavy Meromyosin Studied Using a Fluorescent ATP Analogue[†]

Martina Balaz, Mark Sundberg, Malin Persson, Jan Kvassman, and Alf Månsson*

Department of Chemistry and Biomedical Sciences, University of Kalmar, SE-391 82 Kalmar, Sweden

Received January 31, 2007; Revised Manuscript Received April 3, 2007

ABSTRACT: Biochemical studies in solution and with myosin motor fragments adsorbed to surfaces (in vitro motility assays) are invaluable for elucidation of actomyosin function. However, there is limited understanding of how surface adsorption affects motor properties, e.g., catalytic activity. Here we address this issue by comparing the catalytic activity of heavy meromyosin (HMM) in solution and adsorbed to standard motility assay surfaces [derivatized with trimethylchlorosilane (TMCS)]. For these studies we first characterized the interaction of HMM and actomyosin with the fluorescent ATP analogue adenosine 5′-triphosphate Alexa Fluor 647 2′- (or 3′-) *O*-(*N*-(2-aminoethyl)urethane) hexa(triethylammonium) salt (Alexa-ATP). The data suggest that Alexa-ATP is hydrolyzed by HMM in solution at a slightly higher rate than ATP but with a generally similar mechanism. Furthermore, Alexa-ATP is effective as a fuel for HMM-propelled actin filament sliding. The catalytic activity of HMM on TMCS surfaces was studied using (1) Alexa-ATP in total internal reflection fluorescence (TIRF) spectroscopy experiments and (2) Alexa-ATP and ATP in HPLC-aided ATPase measurements. The results support the hypothesis of different HMM configurations on the surface. However, a dominant proportion of the myosin heads were catalytically active, and their average steady-state hydrolysis rate was slightly higher (with Alexa-ATP) or markedly higher (with ATP) on the surface than in solution. The results are discussed in relation to the use of TMCS surfaces and Alexa-ATP for in vitro motility assays and single molecule studies. Furthermore, we propose a novel TIRF microscopy method to accurately determine the surface density of catalytically active myosin motors.

Muscle contraction is the result of ATP[1]-driven cyclic interactions between myosin II motors and actin filaments (*1*, *2*) (for review see refs *3* and *4*). These interactions may be described by Scheme 1 (*3*, *4*). In this scheme, the myosin catalytic unit is denoted by M, actin by A, and inorganic phosphate by P_i. Rate constants are indicated by lower case letters (k_1−k_5 and k'_1−k'_5) and equilibrium constants by upper case letters (K_1, K'_1, K_T, K_3, K'_3, and K_{DP}). In the absence of actin and at all temperatures used in this study (above 15 °C) the P_i release step is rate limiting for the entire cycle (*5*). In the presence of actin the overall cycle is accelerated more than 2 orders of magnitude, and the rate-limiting step is associated with the binding of M ADP P_i to actin (*3*). Only those actin-binding steps that occur with significant probability during steady-state hydrolysis are included in Scheme 1.

Several important studies of the actomyosin interactions have been performed using the in vitro motility assay (*6*−*13*) and related single molecule mechanical techniques (*14*−*17*). Generally, in these experiments, isolated myosin molecules, or, more often, their proteolytic motor fragments [e.g., heavy meromyosin (HMM)] (*7*), are adsorbed to a glass surface with appropriately modified surface chemistry. After addition of fluorescently labeled actin filaments and a suitable MgATP-containing buffer, actin sliding velocities, force development, etc. can be analyzed (*8*, *11*, *14*, *18*, *19*). Unlike the situation for the entire cycle time, the sliding velocity is generally believed to be rate

---

[†] The work was supported by grants from The Swedish Research Council (Project 621-2004-3449), The Carl Trygger Foundation, The Knowledge Foundation (KK-stiftelsen), The Crafoord Foundation, and The Faculty of Natural Sciences and Engineering, University of Kalmar.

* Corresponding author. E-mail: alf.mansson@hik.se. Telephone: +46-480-446243. Fax: +46-480-446262.

[1] Abbreviations: a40, assay solution without methylcellulose and ionic strength of 40 mM; aMC130, assay solution with methylcellulose and ionic strength of 130 mM; Alexa-ATP, adenosine 5′-triphosphate Alexa Fluor 647 2′- (or 3′-) *O*-(*N*-(2-aminoethyl)urethane) hexa(triethylammonium) salt; ADP, adenosine 5′-diphosphate; APh, Alexa-488 phalloidin; ATP, adenosine 5′-triphosphate; ATPase, adenosine 5′-triphosphatase; AU, arbitrary units; BSA, bovine serum albumin; CV, coefficient of variation; Cy3-EDA-ATP or Cy3-ATP, 2′(3′)-*O*-[*N*-(2-(Cy3-amino)ethyl)carbamoyl]adenosine 5′-triphosphate; Cy5-EDA-ATP or Cy5-ATP, 2′(3′)-*O*-[*N*-(2-(Cy5-amino)ethyl)carbamoyl]adenosine 5′-triphosphate; DTT, dithiothreitol; deoxymant-ATP, 2′-deoxy-2′- (or 3′-) *O*-(*N*-methylanthraniloyl)adenosine 5′-triphosphate; EGTA, ethylene glycol bis(β-aminoethyl ether)-*N*,*N*,*N*′,*N*′-tetraacetic acid; ϵ, extinction coefficient; FEDA-ATP, 2′(3′)-*O*-[*N*-[2-[3-(5-fluoresceinyl)thioureido]-ethyl]carbamoyl]adenosine 5′-triphosphate; FITC, fluorescein isothiocyanate; HMM, heavy meromyosin; HMM^N, heavy meromyosin having their heads tethered to the surface; HMM^C, heavy meromyosin attached to the surface only via the C-terminal part of the S2 domain; HPLC, high-pressure liquid chromatography; mant-ATP, 2′- (or 3′-) *O*-(*N*-methylanthraniloyl)adenosine 5′-triphosphate; MOPS, 3-(*N*-morpholino)propanesulfonic acid; NHS, *N*-hydroxysuccinimide; PBS, phosphate-buffered saline; PMSF, phenylmethanesulfonyl fluoride; QY, quantum yield; RhPh, tetramethylrhodamine phalloidin; r^2, coefficient of determination; SEM, standard error of the mean; SS, steady state; TIRF, total internal reflection fluorescence; TLCK, *N*-α-tosyl-L-lysine chloromethyl ketone; TMCS, trimethylchlorosilane; TRITC, tetramethylrhodamine isothiocyanate; UV, ultraviolet.

10.1021/bi700211u CCC: $37.00

Scheme 1

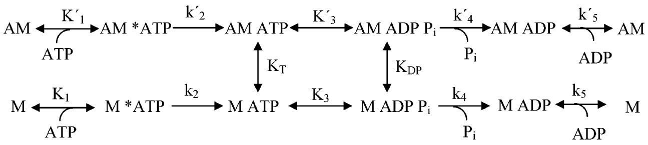

limited by actomyosin dissociation (rate constant k'_5 or k'_2 in Scheme 1) (*20*).

The in vitro motility assay and the single molecule studies are experimental systems with intermediate degrees of structural ordering compared to the three-dimensional disorder in solution studies and the highly ordered arrangement of the muscle proteins in living cells. In order to arrive at a detailed understanding of actomyosin function, the integrated use of all these experimental systems is important. However, currently there is limited insight (*21*) into effects that the systems, themselves, may have on the experimental results. That the effects may be substantial is, for instance, suggested by experiments on micro- and nanopatterned surfaces (*22*−*24*), showing striking differences in HMM-induced actin sliding velocities on neighboring areas with different surface chemistries.

One issue, apart from the motility quality on different surfaces, is whether surface-adsorbed myosin motors have the same ATPase activity as in solution or if there are different HMM configurations with different catalytic activities (*13*, *23*, *25*). This issue, which has not been considered in any detail previously, is of importance for the interpretation both of single molecule experiments and of in vitro motility assay studies in general. In addition, the information should be taken into account when utilizing ATPase assays for the determination of HMM surface density (e.g., refs *13*, *23*, *26*, and *27*).

Any differences in ATPase activity on surfaces and in solution should be possible to address using fluorescent and hydrolyzable ATP analogues (*28*, *29*). Such analogues have previously been used in a limited number of studies (e.g., refs *18*, *30*, *31*) to correlate mechanical and chemical events in single molecule studies and conventional in vitro motility assays. It has appeared that analogues with the fluorescence group linked to the 2′ or 3′ position of ribose (e.g., Cy3-EDA-ATP, Cy5-EDA-ATP, mant-ATP, and deoxymant-ATP) are particularly suitable in this connection since they have a hydrolysis mechanism similar to ATP (*28*). In recent years several analogues of this type have been synthesized, and observation of single fluorescent molecules has become possible (*29*, *32*−*35*). However, there are only a limited number of published original studies [<10 according to a search on Medline and ISI Web of Science (e.g., refs *18*, *30*, and *31*)] that combine in vitro motility assays or single molecule mechanical assays with observation of the turnover of individual fluorescent ATP molecules. One contributing reason may be that some of the ribose-derivatized analogues that are best characterized are not commercially available, e.g., different versions of Cy3- and Cy5-labeled ATP. Furthermore, whereas Cy3-ATP is characterized in greatest detail (*30*, *33*, *34*, *36*), its excitation and emission spectra complicate the combination with standard fluorescent probes for actin [e.g., TRITC-phalloidin and Alexa-488-phalloidin (*37*)]. The spectral properties of Cy5-ATP in this respect are more favorable, but the photostability is lower than for Cy3-ATP (*34*). In addition to Cy5-ATP and Cy3-ADP also mant-ATP has been used frequently in studies of myosin and actomyosin in solution. However, this fluorescent ATP analogue has not been used in fluorescence microscopy studies due to inconvenient excitation in the UV region with resulting poor sensitivity (*35*). Another ribose-derivatized ATP analogue, which does not suffer from some of the above shortcomings, is adenosine 5′-triphosphate Alexa Fluor 647 2′- (or 3′-) *O*-(*N*-(2-aminoethyl)urethane) hexa(triethylammonium) salt ("Alexa-ATP" in the following). Alexa-ATP is commercially available and has a high extinction coefficient and quantum yield and suitable excitation−emission spectra near the infrared region. However, it has been used to a very limited extent in biochemical and biophysical experiments (*38*−*41*). With regard to actomyosin the available studies (*38*, *40*, *41*) have involved the incorporation of Alexa-ATP/ADP into actin filaments and myosin cross-bridges in skinned fibers for correlation of chemical events and force-generating structural changes (see further Discussion). However, there was limited characterization of the hydrolysis properties of Alexa-ATP by myosin in these studies, and one concern is that the relatively large size of Alexa-ATP (molecular weight >2000) may have significant effects on hydrolysis and/or translation of actin filaments by HMM. Another important issue for the potential use of Alexa-ATP in single molecule studies is whether its fluorescence is quenched [e.g., as for fluorescein-EDA-ATP (*35*)] or enhanced [e.g., as for one isomer of Cy3-ATP (*34*−*36*)] upon binding to HMM.

As mentioned above, the mode of surface adsorption of HMM in the in vitro motility assay has been characterized only to a limited extent (*23*, *25*, *42*). One of the few existing studies (*25*) suggests that HMM motors may adsorb in different configurations to nitrocellulose with different actin-propelling and, possibly, different ATP-hydrolyzing capabilities (*23*). Previously (*23*, *43*), we have shown that glass or SiO_2 surfaces, derivatized with trimethylchlorosilane, are suitable substrates for HMM adsorption in the in vitro motility assay. Furthermore, these surfaces, unlike nitrocellulose, have a simple and well-defined chemistry and topography (see Discussion). Also, unlike nitrocellulose, they may be readily nanostructured (*24*, *44*) for the development of nanotechnology-enhanced in vitro motility assays (*21*). Whereas the actomyosin function (sliding velocity, fraction of motile filaments) is as good as on nitrocellulose (*23*, *43*), further characterization of HMM function on TMCS is important for correct interpretation of motility assay and single molecule mechanical studies. Here we first show that Alexa-ATP is quite similar to ATP as a substrate for myosin and actomyosin. Then, using fluorescence spectroscopy, we present evidence for different HMM configurations on TMCS surfaces. A vast majority of these are catalytically active with an activity slightly higher than in solution. This is considered in the Discussion in relation to the usefulness of TMCS-derivatized surfaces and Alexa-ATP in single molecule and in vitro motility assay studies of actomyosin. Preliminary accounts of minor aspects of the present work have been reported (*45*, *46*).

MATERIALS AND METHODS

Chemicals. Tetramethylrhodamine isothiocyanate phalloidin (RhPh), Alexa-488 phalloidin (APh), and adenosine 5′-

triphosphate Alexa Fluor 647 2′- (or 3′-) *O*-(*N*-(2-aminoethyl)-urethane) hexa(triethylammonium) salt (Alexa-ATP) were purchased from Molecular Probes−Invitrogen (Eugene, OR). Whereas the detailed chemical structure of Alexa-ATP is proprietary information (however, see Discussion), it is clear from the chemical name that there are two isomers with the fluorophore attached to either the 2′ or 3′ position of the ribose of ATP. In addition to these two isomers our HPLC data (see below) clearly show the presence of two additional isomers. All other chemicals were of analytical grade and purchased from Merck (Darmstadt, Germany), Sigma-Aldrich (St. Louis, MO), or Fluka and Riedel-de Haën (Seelze, Germany).

Protein Preparations. Myosin was purified from fast skeletal muscle of the rabbit (*47*, *48*). Subsequent to myosin purification heavy meromyosin (HMM) was prepared using TLCK-treated α-chymotrypsin cleavage of myosin (*7*). Immediately after preparation HMM was frozen in liquid nitrogen and then stored at −80 °C for up to 2 years. Prior to HMM usage in experiments each batch was tested in an in vitro motility assay (see below) in order to ensure proper function. During control motility studies, all proteins stored between 1 month and 2 years exhibited high-quality motility with an actin sliding velocity of 10.2 ± 0.5 μm s^{-1} (mean ± SEM, $n = 4$; temperature 29.5 ± 0.5 °C) and a fraction of motile actin filaments ≥80%.

F-actin was purified from rabbit skeletal or bovine cardiac muscle (*49*). Following purification, F-actin was frozen in liquid nitrogen and stored at −80 °C for up to 2 years without any noticeable deterioration in motile function (*37*).

Surface Preparations and Characterization by Contact Angle Measurements. Microscope glass coverslips (No. 0; Menzel-Gläser, Braunschweig, Germany) used for in vitro motility studies were coated with nitrocellulose or derivatized with TMCS (*43*). Total internal reflection fluorescence (TIRF) measurements were performed on UV-fused silica slides (SiO_2; TIRF Technologies, Inc., Harrisburg, PA) silanized with liquid-deposited trimethylchlorosilane (TMCS) (*23*, *43*). Details of the silanization procedure are given in Supporting Information. In order to control for proper TMCS derivatization, the advancing and receding contact angles were measured (*23*) (for details, see Supporting Information).

In Vitro Motility Assays. In vitro motility assays were performed essentially as described previously, with respect to flow cells, incubation procedure, recording of filaments, and analysis of data (*23*, *50*). The average temperature varied between 24.5 and 29.5 °C with a maximal temperature variation of ±1.5 °C in a given experiment. In all in vitro motility experiments the HMM concentration in the incubation solution was 120 μg/mL. An assay solution (aMC130; ionic strength 130 mM) with the following composition was used if not otherwise stated: 10 mM 3-(*N*-morpholino)-propanesulfonic acid (MOPS), pH 7.4, 2 mM $MgCl_2$, 0.1 mM ethylene glycol bis(β-aminoethyl ether)-*N*,*N*,*N*′,*N*′-tetraacetic acid (EGTA), 1 mM Na_2ATP, 10 mM dithiothreitol (DTT), 3 mg/mL glucose, 20 units/mL glucose oxidase, 868 units/mL catalase, 2.5 mM creatine phosphate, 56 units/mL creatine kinase, 0.64% (w/v) methylcellulose, and 105 mM KCl. A major component of the assay solution, as well as of the solutions used in other experiments of this study, is buffer A containing 10 mM MOPS (pH 7.4), 25−30 mM KCl, 10 mM DTT, 1 mM $MgCl_2$, and 0.1 mM K_2-EGTA. When performing motility experiments under low ionic strength conditions, the methylcellulose was omitted and the KCl concentration was reduced to 15 mM, giving an ionic strength of approximately 40 mM (a40 solution).

For experiments at different concentrations of Alexa-ATP and ATP the assay solution was similar to the aMC130 solution but [Alexa-ATP] or [Na_2ATP] was varied between 0.03 and 2 mM. Furthermore, since Alexa-ATP was dissolved in a phosphate buffer, inorganic phosphate (KH_2PO_4−K_2HPO_4, pH 7.4) was also added to the solution with ATP. In a control experiment we found that the presence of inorganic phosphate in the relevant concentrations did not, in itself, affect the sliding velocity. In order to achieve the same free [Mg^{2+}], [P_i], and ionic strength (130 mM) in all assay solutions, [$MgCl_2$] was varied between 1.03 and 3 mM, [KCl] was varied between 20 and 94 mM, and [P_i] was varied between 0.3 and 20 mM. The ionic strength and the free concentration of ATP were calculated using the software winmaxc 3.2 (http://www.stanford.edu/∼cpatton/winmaxc2.html) with stability constants for metal complexes obtained from the NIST Standard Reference Database 46 Version 8.0 (NIST Standard Reference Data, Gaithersburg, MD).

Characterization of Alexa-ATP by HPLC. Alexa-ATP was diluted to 31 μM in buffer A (see above). A 30 μL aliquot of this solution was injected on an HP1090 HPLC system with a Hypersil Gold C-18 column (150 × 4.6 mm i.d., 3 μm particles) and diode array detector recording absorbance at 260 and 598 nm. The flow was 0.8 mL/min of the mobile phase consisting of 75 mM potassium phosphate (pH 5.0) and a gradient of acetonitrile (8% between 0 and 25 min and 30% between 30 and 35 min).

Determination of Steady-State ATPase in Solution Using HPLC. The HMM ATPase with ATP and Alexa-ATP as substrates was investigated by separating the hydrolysis products using HPLC (adapted from refs *51* and *52*). The HMM stock solution was diluted to 100 μg/mL in buffer A. ATP hydrolysis was initiated by mixing 1 volume of HMM stock solution with a stock solution of ATP or Alexa-ATP, yielding final concentrations of 97 μg/mL and 73 μM for HMM and ATP or Alexa-ATP, respectively. Adenosine (final concentration 36 μM in reaction solution) was added as an internal standard to the ATP and Alexa-ATP stock solution in order to allow for more exact measurements of the amount of added ATP or Alexa-ATP. In one control experiment we found that adenosine did not have any significant effect on the myosin ATPase. The hydrolysis was studied at 25 ± 1 °C in a water bath, and the reaction was terminated by adding 1 volume of ice-cold perchloric acid (final concentration 0.3 M). Potassium acetate (final concentration 0.6 M) was added to the mixture, and the precipitate was removed by centrifugation at 9000*g* for 10 min. A fraction of the supernatant was injected into the HPLC system. For separation of ATP and ADP the flow rate was 0.8 mL/min using an aqueous mobile phase with potassium phosphate (75 mM, pH 4.0), tetra-*n*-butylammonium phosphate (1.5 mM), and methanol (13%, v/v). Absorbance was recorded at 260 nm. Alexa-ATP and Alexa-ADP were separated according to the method described above.

When calculating the hydrolysis rates of ATP or Alexa-ATP, HPLC area peaks were normalized to prehydrolysis values. For ATP the prehydrolysis peak for ATP was used for this purpose. For the different isomers of Alexa-ATP, prehydrolysis peaks either for Alexa-ATP or for Alexa-ADP were used (depending on which peaks were best resolved).

Determination of Quantum Yield for Alexa-ATP. *N*-Hydroxysuccinimide- (NHS-) conjugated Cy5 in PBS was used as a reference for the determination of the quantum yield for Alexa-ATP on the assumption that the Cy5 conjugate had the same quantum yield as free Cy5 [0.28 (*53*)]. The quantum yield was determined using a standard procedure as recommended by the manufacturer (Invitrogen−Molecular Probes; see Supporting Information for details).

Kinetic Studies of Fluorescence Changes Associated with the Hydrolysis of Alexa-ATP by HMM in Solution. Measurements were performed in a cuvette using a spectrofluorometer (Fluoromax-3; Jobin Yvon Inc.) equipped with a 150 W xenon lamp and DataMax Software version 2.10 (Jobin Yvon Inc.). Different concentrations of ATP or Alexa-ATP were added to buffer A, followed by addition of HMM (final concentration 0.26 μM) to start the reaction. The concentration of HMM in the stock solution was 1.3 μM, and this solution also contained other components[2] leading to a minor change in composition of the reaction buffer upon addition of HMM. Separate experiments were performed to exclude that this change, in itself, affected the measurements. The temperature in the cuvette was carefully controlled and held at 25 °C. This was important since the fluorescence intensity of Alexa-ATP exhibited strong temperature dependence (see Supporting Information). In the experiments described above the solutions were mixed by turning the cuvette three times, causing a delay of 10 s from addition of HMM to the onset of measurements.

When hydrolysis and binding of ATP were studied by changes in tryptophan fluorescence, the excitation wavelength was set to 295 nm and emission intensity was measured at 340 nm. For studying binding and hydrolysis of Alexa-ATP by HMM, the excitation wavelength was set to 647 nm with emission measured at 668 nm. Increments of 1 s and an integration time of 1 s were used in the measurements, and the excitation and emission slits were set to 1 and 2 nm, respectively.

Separate experiments were performed using a stopped-flow equipment for study of Alexa-ATP binding and Alexa-ADP release from HMM. In these experiments Alexa-ATP binding and Alexa-ADP release from HMM were studied by mixing Alexa-ATP and HMM in a Durrum D110 stopped-flow instrument, rebuilt with leak-tight syringes. Both HMM and Alexa-ATP were dissolved in buffer A, giving final concentrations of 0.25−1.8 and 0.22−0.26 μM of Alexa-ATP and HMM, respectively. The reaction mixtures were excited using light of 648 nm, and the resulting fluorescence was read at right angles through a 666−668 nm cut-on interference filter. A voltage proportional to the photomultiplier signal was transferred to a computer using a PICO ADC-112 virtual instrument as A/D-converter and buffer. The stopped-flow experiments were performed at room temperature (21 °C).

HMM Density on Surfaces Measured by HMM Depletion. The amount of HMM adsorbed to TMCS-derivatized TIRF SiO_2 slides was determined by measuring the HMM depletion from an incubation solution essentially as described earlier (*23*). In brief, flow cells constructed from TMCS-derivatized slides (area ∼5 cm^2 and height ∼100 μm) were incubated with 1 volume of HMM (120 μg/mL) for 2 min. Following incubation the flow cells were rinsed with 20 volumes of buffer B (25 mM imidazole hydrochloride, pH 7.4, 4 mM $MgCl_2$, 1 mM EGTA, 25 mM KCl, and 1 mM DTT). The amount of excess HMM that was recovered in this rinsing procedure was then measured by fluorescence spectroscopy (excitation wavelength, 280 nm, and emission wavelength, 332 nm; SPEX Fluorolog-3-22 spectrofluorometer, Jobin Yvon Instruments, Edison, NJ, used with a DataMax software version 2.10, Jobin Yvon) using a linear standard curve ($r^2 \geq 0.998$) of known HMM concentrations. Finally, the number of adsorbed HMM molecules was calculated from the amount of HMM in the incubation solution before and after incubation.

Steady-State HMM ATPase and Alexa-ATPase on Surfaces. In order to determine the HMM density on the flow-cell surfaces, we measured the amount of HMM depleted from an incubation solution as described above. Subsequently, 1 volume of ATP or Alexa-ATP (0.3 mM) was added to the flow cells and then incubated at 25 ± 0.5 °C for 30−120 min. The nucleotides were added in a modified buffer A (buffer C) that contained 10 mM MOPS (pH 7.4), 1 mM $MgCl_2$, 0.1 mM K_2EGTA, 10 mM DTT, and 3 mM P_i. The KCl concentration was varied between 1 and 1.6 mM in order to adjust the ionic strength to approximately 40 mM. The ATPase reactions were quenched by perfusing the flow cells with 1 volume of ice-cold perchloric acid (0.6 M) and 9 volumes of deionized water. For the blank sample, the HMM molecules on the flow-cell surfaces were first denatured by incubating the cell with 2 volumes of ice-chilled perchloric acid (0.6 M) for 5 min. Following denaturation, the flow cells were incubated with 1 volume of ATP or Alexa-ATP in buffer C and then quickly rinsed with 9 volumes of deionized water. The perfusate from all flow cells was collected and centrifuged. Prior to centrifugation (10 min, 7500 rpm, 4 °C) potassium acetate and adenosine were added to the quenched reaction solutions in a final concentration of approximately 120 mM and 1.25 μM, respectively. Following centrifugation the supernatants were recovered, and the amount of hydrolyzed ATP or Alexa-ATP was determined using HPLC as described above.

TIRF Spectroscopy Studies. The HMM Alexa-ATPase was studied in a total internal reflection fluorescence (TIRF) flow system (BioElectroSpec Inc., Harriburg, PA) integrated into a SPEX Fluorolog-3-22 spectrofluorometer (Jobin Yvon Instruments, Edison, NJ). For data collection DataMax software (version 2.10, Jobin Yvon) was employed. The front surface of the flow cell (where evanescent wave excitation took place) consisted of a TMCS-derivatized fused silica (SiO_2) slide coupled via glycerol to a fused silica prism. A thermostatic circulator was connected to the back metal (stainless steel) block of the TIRF flow cell where a bead probe was placed to monitor the temperature during the experiments. TIRF experiments were performed at 15 or 25 °C with a maximum variation in temperature of ±0.5 °C within a given experiment. The assembled TIRF flow cell had a height of ∼100 μm and a surface area of 3.4 cm^2, giving a volume of ∼34 μL. Unless otherwise stated, a

---

[2] KCl (50 mM), $MgCl_2$ (3 mM), $NaHCO_3$ (0.1 mM), EGTA (0.1 mM), DTT (2.5 mM), imidazole hydrochloride (1 mM), sucrose (2 mg/mL; for cryoprotection). Trace amounts of inactivated chymotrypsin (1 μg/mL) and PMSF (0.1 μM) are also present.

syringe pump 50300 (Kloehn, Las Vegas, NV) was used for injection of solutions into the flow cell. For protein fluorescence the excitation and emission slits were set to 280 and 332 nm, respectively. The excitation and emission wavelengths for the monitoring of Alexa-ATP fluorescence were set to 649 and 666 nm, respectively. The emission intensity was measured with corrections for intensity fluctuations in the 450 W xenon lamp. For protein binding studies the time scans were obtained with an increment of 2 s and an integration time of 1 s. Time scans for studies of the Alexa-ATP TIRF fluorescence were set at an increment of 0.5 s and an integration time of 0.5 s. Control experiments to test the photostability of Alexa-ATP showed no difference in photobleaching when the fluorescent ATP was subjected to evanescent wave excitation for a time period of 700 s using an excitation slit corresponding to 1 or 2 nm and a time increment of 0.5 s (shutter open between measured points) or 7 s (shutter closed between measured points). To obtain good excitation of protein and fluorescent ATP, without photobleaching effects, the excitation slit was set at a 2 nm spectral bandwidth. In order to ensure proper collection of emitted light, the emission slit was set at a spectral bandwidth of 6 nm.

During TIRF experiments a TMCS-derivatized SiO_2 surface was mounted into the TIRF flow cell and incubated with HMM followed by Alexa-ATP and various rinsing steps (see Supporting Information for further details). In one of the rinsing steps 5 μM regular ATP was included to displace any bound Alexa-nucleotide. We refrained from using higher ATP concentration even if more effective displacement of the Alexa-nucleotide would be expected. The reason is the increased difficulty of removing all unlabeled nucleotide with complications in the interpretation of Alexa-ATP signals in subsequent runs using the same flow cell.

The decaying phase of the Alexa-ATP fluorescence signal upon rinsing was analyzed by nonlinear regression. The number of exponential processes in the data was determined in a pilot study employing semilogarithmic plots of the data. A regression line was first fitted to the final linear part of the curve yielding the amplitude and the rate constant of the slowest exponential process. The equation for this process was then subtracted from data yielding a new multiexponential function. The process was repeated until the multiexponential function was completely stripped (i.e., equaled zero).

Stripping of data yielded a multiexponential equation with five exponential components. However, we found that a triple exponential function gave a satisfactory fit to the data. The fastest exponential phase was associated with the rinsing process, and this phase was disregarded by not starting the fitting procedure until rinsing was complete. Second, one slow exponential phase with very low amplitude was disregarded. When fitting the triple exponential function to the data, the amplitude (A_3) and rate constant (k_3) for the slowest remaining phase were first determined from linear regression using semilogarithmic plots. These values were then held constant in the subsequent fitting of the entire equation using nonlinear regression. In this fitting procedure the parameter values in eq 1 (obtained in a pilot study) were used as initial values (with A_3 and k_3 as constants determined in each experiment).

$$y = 0.377e^{-0.071t} + 0.155e^{-0.024t} + A_3e^{k_3t} \tag{1}$$

In this equation the amplitudes were normalized to the maximum fluorescence intensity during incubation with Alexa-ATP. For short incubations (15−170 s) this value occurred just prior to rinse with Alexa-ATP-free solution ($t = 0$ s). For long incubations, where hydrolysis of Alexa-ATP was allowed to be completed, the maximum value was also used for normalization, but in this case it occurred more than 1000 s prior to the rinsing (see below; Figure 5). Due to these normalization procedures the amplitudes for short runs summed up to a value between 0.54 and 0.66 at 3 μM Alexa-ATP. The remaining fraction (0.34−0.46) was accounted for by the contribution from nonspecific binding and Alexa-ATP in the bulk. For long runs with complete hydrolysis the amplitudes for the exponential phases summed up to a value between 0.08 and 0.13 as further considered in the Results and Discussion.

Another set of initial values was used for the fitting of a triple exponential function to data obtained at 15 °C corresponding to the equation:

$$y = 0.172e^{-0.019t} + 0.089e^{-0.0039t} + A_3e^{k_3t} \tag{2}$$

Numerical Solution of Differential Equations. Systems of differential equations were solved by numerical integration using the fourth-order Runge−Kutta−Fehlberg method implemented in the software Simnon (v.1.3; SSPA, Gothenburg, Sweden). Increasing the time step in the numerical integration 10 times did not appreciably affect the outcome of the simulations.

Statistical Analysis and Graphics. Statistical analysis, including linear and nonlinear regression (Levenberg−Marquardt algorithm), was performed using the GraphPad Prism software (version 4.0; GraphPad Software, San Diego, CA). Unless otherwise stated data are given as the mean ± standard error of the mean (SEM). The table of contents graphic was rendered using the free software Povray 3.6 (http://www.povray.org/).

RESULTS

HPLC-Aided Study of Steady-State Hydrolysis of ATP and Alexa-ATP in Solution. The degree of separation obtained for the isomers of Alexa-ATP enabled quantification of the composition and of the ATPase for the different isomers. Four different hydrolyzable isomers were found (Figure 1A; see further discussion) with a similar area for all isomer peaks (for details see Supporting Information). Separation of ATP and ADP before and 40 min after the onset of steady-state hydrolysis by HMM is shown for comparison in Figure 1B.

It is important to note that, in consistency with the information from the manufacturer, we did not detect any significant (>1%) impurity (e.g., ATP or ADP) in the Alexa-ATP samples.

The HMM-catalyzed hydrolysis rates of the Alexa-ATP isomers differed slightly (Table 1). When tested with a given HMM preparation, the k_{cat} value for the HMM ATPase averaged over all Alexa-ATP isomers (0.0345 ± 0.001 s^{-1}; $n = 2$ replicates, Figure 1C) was 1.54 times greater than that for ATP (0.0224 ± 0.001 s^{-1}; $n = 3$, Figure 1C). Studies using one other HMM preparation gave similar results.

Kinetic Studies of Fluorescence Changes Associated with the Hydrolysis of Alexa-ATP by HMM in Solution. The quantum yield for Alexa-ATP in buffer A was approximately 0.39.

Figure 2A illustrates changes in fluorescence emission upon mixing (first arrow, I) a slight excess of Alexa-ATP (final concentration 0.7 μM) with HMM (0.26 μM; final concentration). Subsequently (after about 500 s, second arrow, II), Alexa-ADP was displaced from the active site by addition of ATP (0.25 mM). It is clear from the trace in Figure 2A that binding of Alexa-ATP to HMM quenched the fluorescence. On basis of an active site concentration of 0.52 μM the quenching could be estimated to be in the range 20−30% in different experiments (after correction for a small nonlinearity of the intensity-concentration relation for Alexa-ATP; Supporting information). In addition, we also observed quenching of the HMM intrinsic fluorescence upon binding of Alexa-ATP to the catalytic site of HMM (data not shown).

The decrease in fluorescence associated with the binding of Alexa-ATP (first arrow in Figure 2A) is shown on an expanded time scale in the left inset (I) of Figure 2A. This time course can be approximated by a single exponential function ($r^2 = 0.98$). However, in order to obtain the initial rate, to allow estimation of K_1k_2, double exponential functions were fitted to the data. For this purpose we mixed Alexa-ATP (final concentration 1.8 μM) with HMM (final concentrations 0.26 μM; data not shown). The higher Alexa-ATP concentration reduced the relative change in nucleotide concentration during binding. The rate constants obtained in such fits were $k_{12}{}^{\text{fast}} = 3.88 \pm 0.22$ s^{-1} and $k_{12}{}^{\text{slow}} = 0.80 \pm 0.12$ s^{-1} (three replicate runs) with corresponding amplitudes of 77% and 23%, respectively. From the dominating phase (representing the initial rate) a value of 2 μM^{-1} s^{-1} was obtained for the second-order rate constant of Alexa-ATP binding to HMM.

The next part of the fluorescence trace (within the dashed box in Figure 2A) was associated with turnover of Alexa-ATP as considered in detail below. Following this phase (>100 s after mixing of Alexa-ATP and HMM; after completed hydrolysis) the fluorescence intensity was still below the value for free Alexa-ATP, and it did not change further with time. Thus, linear regression analysis applied to the trace from 610 to 1010 s in Figure 2A gave a nonsignificant negative slope.

Within 10 s after addition of 0.25 mM ATP (second arrow in Figure 2A) the signal was shifted back to be virtually identical to the value for free Alexa-ATP. The <1% difference from that value is accounted for by the photobleaching of Alexa-ATP (~0.6% during a 500 s observation period). This result is consistent with identical fluorescence intensities of free Alexa-ATP and Alexa-ADP. The time course of the increase in fluorescence intensity upon addition of ATP is illustrated in the right inset (II) of Figure 2A. The fluorescence recovery could be approximated by a single exponential function with a half-time of 0.4 s. Better fits were obtained using a double exponential function, giving rate constants of 5.9 ± 0.1 and 1.2 ± 0.03 s^{-1} (three replicate stopped-flow runs) for the fast and slow phase with similar amplitudes for both phases.

As mentioned above, the part of the fluorescence trace within the dashed box in Figure 2A (denoted "*B*") was associated with turnover of Alexa-ATP. It is illustrated, on a faster time base, in Figure 2B together with the results of a similar experiment using 1.3 μM Alexa-ATP. The flat

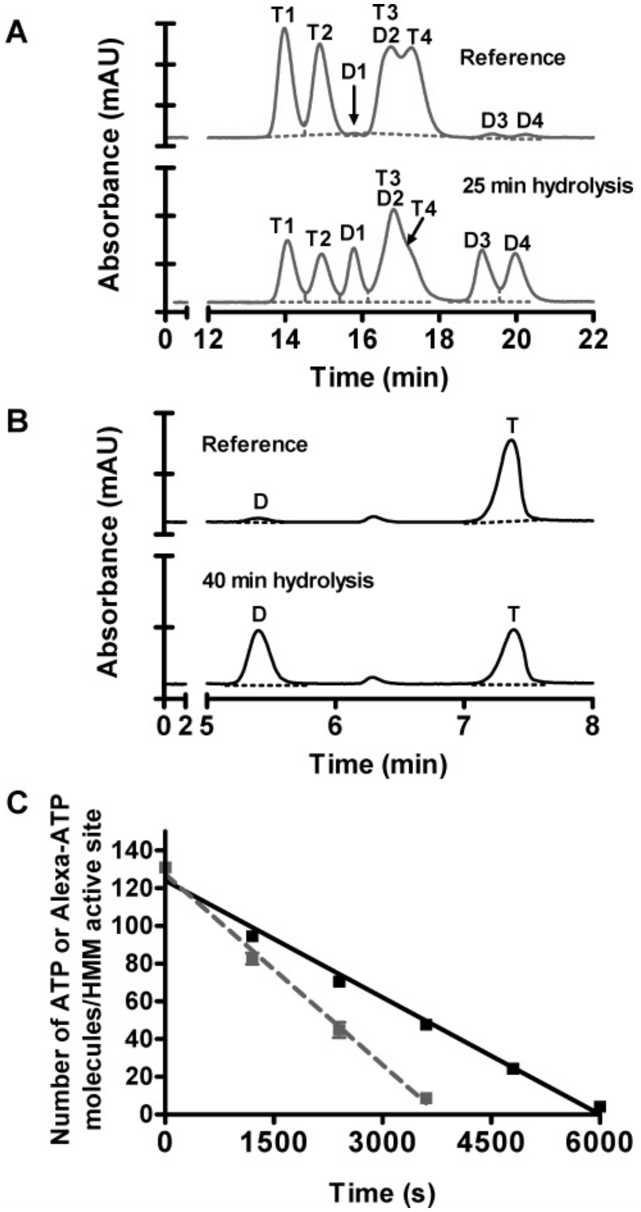

FIGURE 1: Steady-state hydrolysis in solution of ATP and Alexa-ATP studied by HPLC. (A) HPLC chromatograms of Alexa-ATP and Alexa-ADP isomers (absorbance at 598 nm). The top trace shows the reference before onset of hydrolysis ($t = 0$ min). The bottom trace represents the composition of nucleotides 25 min after the onset of hydrolysis. Alexa-ATP peaks are denoted T1−T4 while Alexa-ADP peaks are denoted D1−D4 (see Supporting Information). (B) HPLC chromatograms showing the composition of ATP and ADP (absorbance at 260 nm) in the reference sample ($t = 0$ min, top trace) and following 40 min of hydrolysis ($t = 40$ min, bottom trace). The peak labeled T is attributed to ATP while the peak labeled D is attributed to ADP. The unlabeled peak was constant in size throughout the experiments. Separate studies show that this peak is not related to ATP (data not shown). Dashed lines in (A) and (B) indicate limits for integration to calculate peak areas. One tick interval in (A) and (B) equals 25 mAU. (C) Data showing the mean number of remaining ATP (black symbols) and Alexa-ATP (gray symbols) molecules per active site of HMM plotted against time. Average values of two experiments. Regression lines fitted to the data are shown by a full black line for ATP (slope = −0.021 s^{-1}, $r^2 = 0.99$, $n = 2$) and a dashed gray line for Alexa-ATP (slope = −0.034 s^{-1}, $r^2 = 0.99$, $n = 2$). If no error bars are shown; the SEM is smaller than the size of the symbol. Temperature: 25 ± 1 °C.

Table 1: Steady-State HMM-Catalyzed Hydrolysis of ATP and Different Alexa-ATP Isomers[a]

	regular ATP	Alexa-ATP isomer 1	Alexa-ATP isomer 2	Alexa-ATP isomer 3	Alexa-ATP isomer 4
k_{cat} (s^{-1})	0.022 ± 0.001 ($n = 3$)	0.032 ± 0.001 ($n = 2$)	0.036 ± 0.001 ($n = 2$)	0.034 ± 0.001 ($n = 2$)	0.035 ± 0.002 ($n = 2$)

[a] Data (mean ± SEM) from two to three replicate experiments using one HMM preparation.

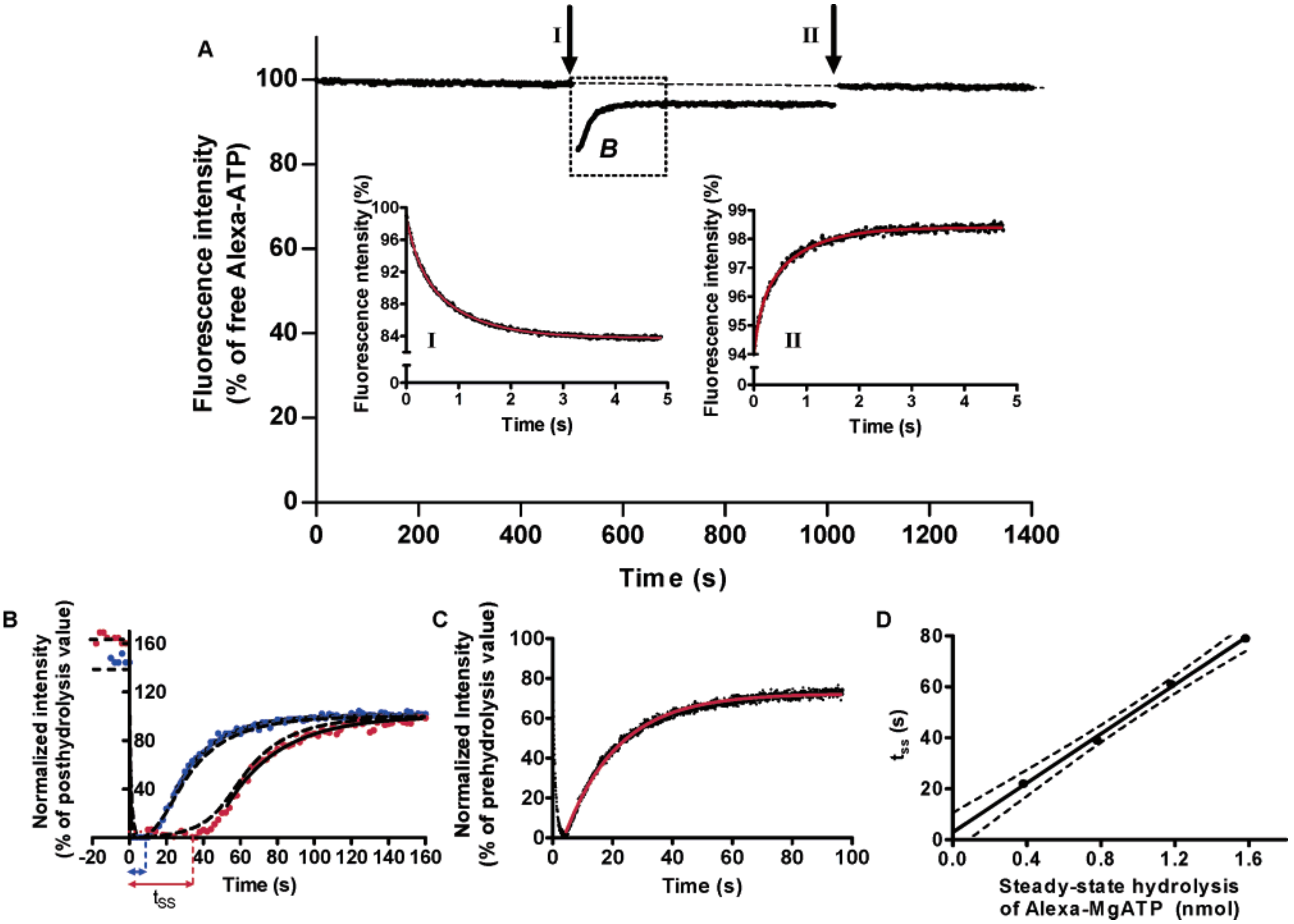

FIGURE 2: Changes in fluorescence upon mixing of Alexa-ATP and HMM in solution. (A) HMM (0.26 μM, final concentration) added to Alexa-ATP (0.7 μM, final concentration) at the first arrow (I), followed by hydrolysis and subsequent addition of 0.25 mM regular ATP (second arrow, II). The part of the trace enclosed in the dashed square (denoted *B*) is illustrated in greater detail in panel B. The nearly horizontal broken line in (A) indicates the slope of the fluorescence signal before mixing with HMM to illustrate the negligible photobleaching of Alexa-ATP. The addition of HMM diluted the Alexa-ATP by 16%, and the trace before mixing has been shifted to account for this effect. Insets show stopped-flow records from another experiment illustrating the first 5 s of the fluorescence signal immediately after mixing HMM with Alexa-ATP (inset I, first arrow) and immediately after adding regular ATP (inset II, second arrow). The red lines are double exponential fits to the data (see text). Data in the insets were obtained with other gain/photomultiplier settings than the data in the main panel A. However, for the purpose of clarity, they have been scaled to fit the relative changes observed at arrows I and II, respectively. (B) Details of the trace within the dashed square (denoted *B*) in panel A. In addition to the trace for 0.7 μM Alexa-ATP in (A) (blue dots), the result of mixing HMM (0.26 μM) with Alexa-ATP (final concentration 1.3 μM, black dots) is illustrated. At the time of mixing ($t = 0$ s) the fluorescence intensity dropped from premixing values indicated at pre-zero times. The postmixing fluorescence level was maintained at a minimal value for a time period t_{ss} during which all active sites of HMM were presumed to be occupied by Alexa-ATP. After this time period there was first a brief sigmoidal phase followed by an increase in fluorescence intensity according to a single exponential function (full black lines; see text). The dashed lines represent simulation of the data (Scheme 1) using the parameter values in Table 4. In order to account for the difference between the prehydrolysis and posthydrolysis intensities, k_{-5} was set to 2 $\mu M^{-1}\ s^{-1}$. The myosin head density was assumed to be 10% lower than the nominal value as motivated in the text. In this simulation, the fluorescence was assumed to be quenched by 25% upon binding of Alexa-ATP and Alexa-ADP to the active site of HMM. The excitation wavelength is 647 nm and the emission wavelength is 668 nm in (A) and (B). (C) Stopped-flow data showing early changes in fluorescence after mixing HMM (final concentration 0.26 μM) with Alexa-ATP (final concentration 0.25 μM). The red line represents the single exponential function fitted to the recovery of fluorescence during single turnover of Alexa-ATP (see further text). (D) The time period, t_{ss} (see text and above), for the steady-state hydrolysis plotted against the amount of Alexa-ATP that was hydrolyzed. The full line and dashed lines represent the regression line and 95% confidence limits, respectively. $T = 25$ °C except for the stopped-flow records (insets in panel A, 21 °C).

fluorescence trace during steady-state hydrolysis (time, t_{ss}) and the relatively abrupt onset of the subsequent exponential increase in fluorescence intensity suggest that the concentrations of Alexa-ATP are above K_M. Simulations based on the kinetic Scheme 1 (dashed lines in Figure 2B) gave reasonable fits to the data for both 0.7 and 1.3 μM Alexa-ATP using the same numerical values of the rate constants (Appendix, Table 4).

Assuming that the concentration of active sites ([HMM sites]$_N$) $\gg K_M$, the observed rate constant (k_{obs}) of the exponential increase in fluorescence (Figure 2B) would be approximately equal to k_{cat}. This value was 0.047 ± 0.001,

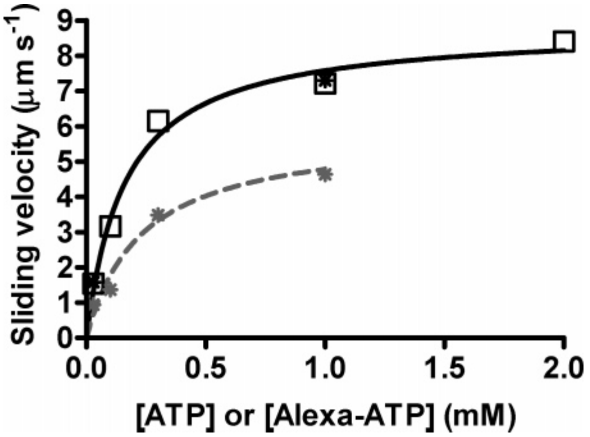

FIGURE 3: Velocities of smoothly sliding actin filaments plotted against ATP (black symbols) and Alexa-ATP (gray symbols) concentrations. Open squares indicate automatic tracking of filaments, and asterisks indicate manual tracking. For automatic and manual tracking of smoothly sliding filaments, coefficients of variation (CV) of the frame−frame velocity <0.2 and <0.3, respectively, were required for acceptance of filament paths for analysis. Note the complete overlap of data obtained by manual and automatic tracking at 0.03 and 1 mM regular ATP. Rectangular hyperbolic curves were fitted to the data for ATP (full black line; $V_{max} \approx 8.81$ μm s^{-1}, $K_m \approx 0.16$ mM, and $r^2 = 0.91$) and Alexa-ATP (dashed gray line; $V_{max} \approx 5.90$ μm s^{-1}, $K_m \approx 0.23$ mM, and $r^2 = 0.93$). The mean velocity of smoothly sliding filaments was calculated from at least 36 filament paths for each data point. If no error bars are shown, the SEM is smaller than the size of the symbol. Data were obtained using TMCS-derivatized glass coverslips. Temperature = 25.4 ± 0.4 °C.

0.049 ± 0.0009, and 0.049 ± 0.0014 s^{-1} in three experiments where a slight excess of Alexa-ATP (0.7−0.9 μM in final concentration) was mixed with HMM (0.26 μM). One stopped-flow experiment under single-turnover conditions (Figure 2C) gave a similar result with $k_{obs} = 0.056 \pm 0.0002$ s^{-1}. The fit to a single exponential function was good ($r^2 = 0.985-0.996$) in all of these four experiments (e.g., Figure 2B,C). Additionally, there was no significant deviation between the experimental data and the single exponential model ($p > 0.09$ in run's test; exclusion of initial sigmoidal phase) in the three experiments where the run's test was applicable. Most importantly, as was also clear by detailed inspection of Figure 2A, there was no sign of very slow phases (half-time around 100 s and more) similar to those observed with HMM adsorbed to surfaces (see below).

The time period, t_{ss} (defined in Figure 2B), may be related to the amount of hydrolyzed Alexa-ATP ([Alexa-ATP]$_0$ − [HMM sites]$_N$) during steady state according to the relationship:

$$t_{ss} = \frac{[\text{Alexa-ATP}]_0 - [\text{HMM sites}]_N}{k_{cat}[\text{HMM sites}]_N} \quad (3)$$

where [Alexa-ATP]$_0$ is the concentration of Alexa-ATP before the onset of hydrolysis.

This relationship provides an alternative way of calculating k_{cat}, giving a value of $k_{obs}{}^{SS} = 0.040 \pm 0.001$ s^{-1} (same in each of two replicate experiments). This value was slightly lower than k_{obs}, an effect that (taking variability into account) could be explained, e.g., by a slight (∼10%) systematic overestimation of the active HMM concentration, possibly combined with a small underestimation of the Alexa-ATP concentration. Importantly, however, the data are not readily consistent with an overestimation of the Alexa-ATP concentration, thus providing further evidence that the entire fraction of the analogue was hydrolyzable.

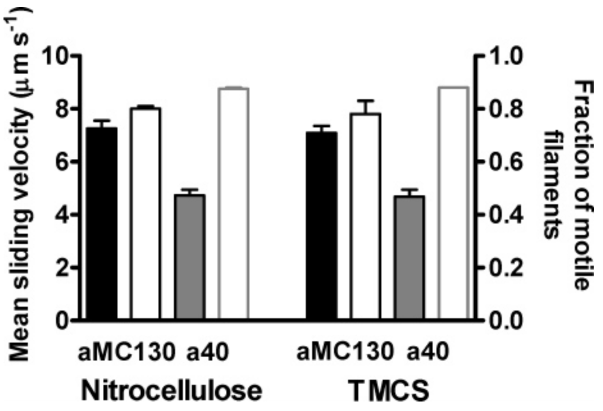

FIGURE 4: In vitro motility assay data comparing actomyosin function on nitrocellulose and TMCS-derivatized fused silica (SiO_2) TIRF slides. Mean sliding velocities (filled bars, left vertical axis) and the fraction of motile filaments (open bars, right vertical axis) were studied in aMC130 (black) and a40 (gray) solutions (1 mM ATP). Data were obtained in two experiments with different batches of surfaces, HMM, and assay solutions. Velocities of smoothly sliding filaments (CV < 0.2) are based on at least 44 filament paths in each experiment. Temperature = 25.8 ± 1.25 °C.

The hydrolysis of ATP by HMM was studied through changes in tryptophan fluorescence. These measurements gave values of k_{obs} and $k_{obs}{}^{SS}$ of 0.026 ± 0.001 and 0.024 ± 0.001 s^{-1}, respectively.

Comparison of Alexa-ATP and ATP as Substrates in the in Vitro Motility Assay. To test whether Alexa-ATP and ATP differ in their ability to support HMM-induced sliding of actin filaments, we performed experiments using different nucleotide concentrations (Figure 3). Using TMCS-derivatized glass coverslips, we found a 33% lower sliding velocity (V_{max}) with Alexa-ATP than with ATP, at saturating substrate concentration. Furthermore, Alexa-ATP gave a 30% higher K_m value. One additional in vitro motility assay experiment at ATP and Alexa-ATP concentrations of 0.03 mM gave 13% lower sliding velocity with Alexa-ATP. Due to the high fluorescence background, the in vitro motility study was limited to Alexa-ATP concentrations ≤1 mM, and filament tracking was performed manually in these experiments. There was no significant difference in actin sliding velocities between the manual and automatic tracking procedure as indicated by comparison at two different concentrations of ATP (Figure 3).

Characterization of TMCS Surfaces Used for TIRF Spectroscopy Studies. Contact angle measurements on TMCS-derivatized SiO_2 surfaces gave an advancing contact angle of 69.1 ± 1.0° ($n = 8$ batches). No significant difference was found between the advancing and receding angle, indicating a homogeneous silanization.

TMCS-derivatized SiO_2 surfaces were further characterized by studying their ability to support actomyosin function in vitro. The results (Figure 4) show no difference in mean actin sliding velocity or fraction of motile actin filaments between the TMCS-derivatized SiO_2 surfaces and standard nitrocellulose surfaces.

Hydrolysis of Alexa-ATP on TMCS Surfaces. The turnover of Alexa-ATP by HMM adsorbed to a TMCS surface was

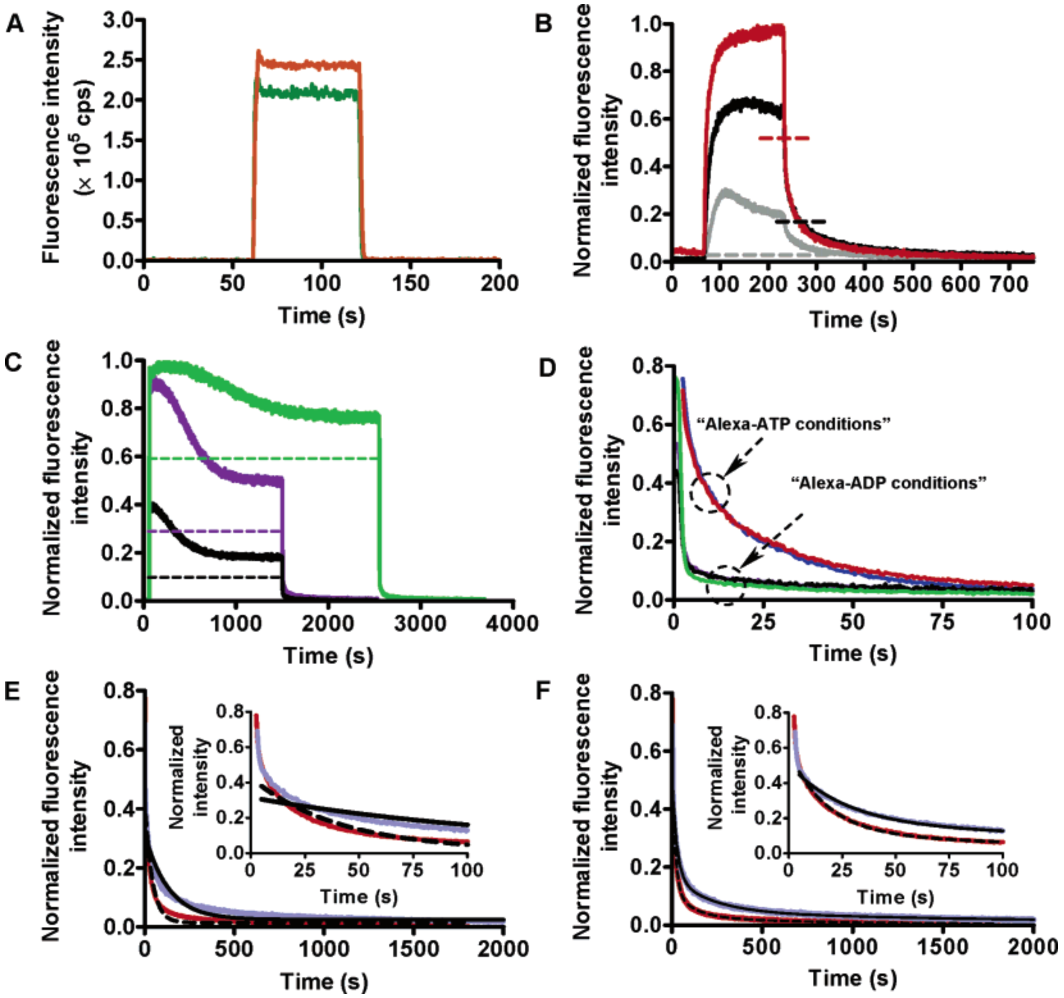

FIGURE 5: Total internal reflection fluorescence (TIRF) transients due to Alexa-ATP incubations of the TIRF flow cell prior to, or following, adsorption of HMM to the TMCS surface. (A) Comparison of total fluorescence amplitudes for bulk (dark green, no HMM on surface) and bulk contribution plus nonspecific binding of Alexa-ATP to HMM (orange). The TIRF flow cell was incubated with 3 μM Alexa-ATP between 60 and 125 s. Nonspecific binding of Alexa-ATP to HMM was studied by adding Alexa-ATP after HMM incubation while blocking active sites of the proteins with 5 mM ATP. (B) Normalized fluorescence intensity plotted against time for TIRF flow-cell injections with solutions containing 0.3 μM (light gray lower trace), 1 μM (black middle trace), and 3 μM (red upper trace) Alexa-ATP. The surfaces had been preincubated with HMM at 120 μg/mL. The infusion of Alexa-ATP solutions was of slower rate (312.5 μL min^{-1}) compared to other experiments of the present study. Following injection, each Alexa-ATP solution was incubated for 170 s followed by quick rinsing (at time $t = 240$ s). Note the superposition of signals for 1 and 3 μM Alexa-ATP after rinsing and removal of bulk fluorescence and nonspecifically bound Alexa-ATP. Straight dashed lines indicate estimated fluorescence intensity levels for Alex-ATP attributed to bulk effects and nonspecific binding. (C) Prolonged incubations of the TIRF cell with, in order, 3 μM (full violet line), 1 μM (full black line), and 6 μM (full green line) Alexa-ATP. The cell had been preincubated with HMM at 120 μg/mL before the first injection of Alexa-ATP. The HMM density on the TMCS-derivatized TIRF slide decreased with time as indicated by changes in intrinsic fluorescence intensity attributed to the surface-adsorbed HMM. If the HMM density before the first injection of Alexa-ATP (3 μM) was set to 100%, the density was 90% and 80% before injection with 1 and 6 μM Alexa-ATP, respectively. The straight dashed lines indicate the fraction of the fluorescence intensity that can be attributed to bulk effects at 1 (black), 3 (violet), and 6 (green) μM Alexa-ATP. (D) Fluorescence decay after rinsing with Alexa-ATP-free solution. The data in (C) were replotted with the same color code to illustrate the effect of rinsing with predominantly Alexa-ADP at the active site of HMM (Alexa-ADP conditions; see text). This condition is compared to the effect of rinsing 15 s (blue) and 90 s (red) after the first Alexa-ATP injection (Alexa-ATP conditions; data not shown in panel C). The data have been normalized to the maximum fluorescence intensity observed during each given incubation. Note that a large and relatively fast phase of fluorescence decay is only present in the Alexa-ATP conditions. Also note the similarity between the Alexa-ADP conditions for different concentrations of Alexa-ATP. (E, F) Decaying phase of the fluorescence signal (Alexa-ATP conditions) upon rapid rinsing with Alexa-ATP-free solution under Alexa-ATP conditions. Data were obtained at 25 ± 0.5 °C (red trace: mean values of two traces in the same experiment) and 15 ± 0.5 °C (light blue trace: one trace). The two traces at 25 °C were obtained before and after the trace at 15 °C. The inset shows the first 100 s of the decay. (E) Single exponential function fitted by nonlinear regression shown as a dashed black line for data at 25 ± 0.5 °C ($y = 0.41e^{-0.025t}$ and $r^2 = 0.93$) and full black line for data at 15 ± 0.5 °C ($y = 0.29e^{-0.0076t}$ and $r^2 = 0.904$). (F) Triple exponential function fitted by nonlinear regression shown as a dashed black line for data at 25 ± 0.5 °C ($y = 0.46e^{-0.058t} + 0.095e^{-0.0084t} + 0.025e^{-0.00090t}$ and $r^2 = 0.998$) and full black line for data at 15 ± 0.5 °C ($y = 0.3409e^{-0.038t} + 0.12e^{-0.0046t} + 0.045e^{-0.00043t}$ and $r^2 = 0.996$).

assessed using a TIRF spectroscopy setup. The HMM incubation concentration of 120 μg/mL gave an average HMM density on the TMCS-derivatized TIRF slides of 5400 ± 400 μm^{-2} ($n = 5$ batches). This value was estimated from HMM depletion of the incubation solution.

When a TIRF cell was incubated with Alexa-ATP in the absence of HMM on the surface, a significant fluorescence signal was still detected (Figure 5A). This was due to the presence of Alexa-ATP molecules in the bulk volume within the region of evanescent wave excitation close to the surface.

Table 2: Triple Exponential Fits to the Decaying Phase of Fluorescence in One TIRF Experiment at Different Alexa-ATP Concentrations and Incubation Times[a]

	k_1 (s^{-1})	k_2 (s^{-1})	k_3 (s^{-1})	A_1 (%)	A_2 (%)	A_3 (%)
Alexa-ATP condition						
3 μM 15 s incubation	0.071 ± 0.0009	0.018 ± 0.0003	0.0012 ± 0.0001	48 ± 0.3	16 ± 0.4	1.3 ± 0.06
3 μM 90 s incubation	0.065 ± 0.0007	0.014 ± 0.0002	0.0011 ± 0.00003	44 ± 0.2	14 ± 0.2	1.9 ± 0.04
Alexa-ADP condition						
1 μM 1440 s incubation	0.073 ± 0.006	0.011 ± 0.0005	0.00079 ± 0.00003	6.4 ± 0.3	3.2 ± 0.2	2.6 ± 0.06
3 μM 1440 s incubation	0.068 ± 0.002	0.010 ± 0.0002	0.00070 ± 0.00002	7.8 ± 0.1	3.1 ± 0.09	2.1 ± 0.03
6 μM 2490 s incubation	0.056 ± 0.002	0.010 ± 0.0004	0.00065 ± 0.00002	5.3 ± 0.1	2.2 ± 0.1	1.6 ± 0.02

[a] Data given as the mean ± SEM. Estimates of SEM obtained in the linear and nonlinear regressions.

It is also evident from Figure 5A that there was no nonspecific binding of Alexa-ATP to the TMCS surface. Thus, the fluorescence signal, in the absence of HMM, decayed to zero immediately upon removal of Alexa-ATP.

When the cell was subsequently incubated with HMM followed by Alexa-ATP, in the presence of 5 mM ATP (to block the active sites of HMM), the amplitude of the fluorescence signal was similar to that for the pure bulk contribution. This suggests very low nonspecific binding of Alexa-ATP outside the active site of HMM. Moreover, it is also evident from Figure 5A that any Alexa-ATP nonspecifically bound to HMM detached very rapidly upon removal of Alexa-ATP from the bulk. In four experiments at 3 μM Alexa-ATP the fluorescence signal attributed to bulk effects and nonspecific binding of Alexa-ATP amounted to 48% ± 4.6% of the total fluorescence signal ($n = 7$ using four HMM/surface batch combinations). The signal that was attributed to the sum of nonspecific binding and bulk effects was roughly proportional to the Alexa-ATP concentration (within the range 1−6 μM) as studied in a separate control experiment (data not shown).

When experiments were performed to study the Alexa-ATPase activity of HMM molecules on the TMCS surface, it was important to ensure saturation of HMM with Alexa-ATP. Therefore, control experiments were performed where the TIRF flow cell was injected with buffer A containing different concentrations of Alexa-ATP. One representative experiment with Alexa-ATP concentrations of 0.3, 1, or 3 μM is illustrated in Figure 5B. As can be seen here Alexa-ATP concentrations in the range 1−3 μM (middle and upper trace in Figure 5B) and above ensured near saturation (relatively constant fluorescence intensities) of the active sites of HMM during the entire time period of Alexa-ATP incubation. This is consistent with the total active site concentration in the TIRF flow cell that was 0.18 μM (in the case of HMM adsorption only to the TIRF slide)[3] or 0.36 μM (in the case of adsorption also to the stainless steel roof of the TIRF flow cell). The reduced TIRF signal at reduced Alexa-ATP concentrations in Figure 5B was mainly attributed to a lower bulk concentration and lower nonspecific binding of Alexa-ATP (indicated by dashed lines in Figure 5B).

The almost complete saturation of the active sites with Alexa-ATP, at incubation concentrations above 1 μM, is also clearly illustrated by the good superposition of the signals for 1 and 3 μM Alexa-ATP after the first 5 s of rinsing. At this point Alexa-ATP in the bulk had been removed as well as the nonspecifically bound nucleotide analogue (cf. Figure 5A).

The good superposition of the remaining parts of the fluorescence decay at 1 and 3 μM Alexa-ATP also suggests that there was no significant difference in the single-turnover rate under these conditions. Due to the different ratios of Alexa-ATP/Alexa-ADP at the point of rinsing in the two cases, this suggests that Alexa-ADP does not significantly inhibit the hydrolysis.

At lower ATP analogue concentrations the signal decayed with time (i.e., 0.3 μM, lower trace Figure 5B) during Alexa-ATP incubation. As expected, a similar decay with time was observed at higher Alexa-ATP concentration if the observation period was sufficiently prolonged (Figure 5C). The decay in the fluorescence signal with time during the steady-state hydrolysis in these experiments represents the decrease in Alexa-ATP concentration (with increase in Alexa-ADP concentration) and thereby a decreased occupation of the active sites with fluorescent nucleotide. This interpretation is consistent with computer simulations below. The time courses of the fluorescence signal upon rinsing in the experiments with prolonged incubations (Figure 5C) are illustrated in some detail in Figure 5D and considered further below.

The decay of the fluorescence signal upon rinsing early (within 15−170 s) after incubation with Alexa-ATP (e.g., Figure 5B) is illustrated on an expanded time in Figure 5E,F. Here the decaying phase was compared at 15 and 25 °C. As can be seen in Figure 5E, the data could not be well fitted by a single exponential function. Instead, a triple exponential function was used (Figure 5F) as described in the Materials and Methods section. It can be seen that the rate of the decay in the fluorescence signal was reduced by a reduction in temperature. Fittings to triple exponential functions gave markedly lower rates of all exponential processes at 15 °C compared to the situation at 25 °C. Thus, at 15 °C, $k_1 = 0.038 \pm 0.0002$ s^{-1}, $k_2 = 0.0046 \pm 0.00002$ s^{-1}, and $k_3 = 0.00043 \pm 0.000003$ s^{-1}, whereas at 25 °C, $k_1 = 0.058 \pm 0.0003$ s^{-1}, $k_2 = 0.0084 \pm 0.0008$ s^{-1}, and $k_3 = 0.0009 \pm 0.00001$ s^{-1}, using the same HMM/surface combination. The estimates of the standard errors of the mean in these cases were obtained in the nonlinear regression procedure. The fastest exponential process contributed to 79% and 67% of the total hydrolysis signal at 25 and 15 °C, respectively.

The above results are all consistent with the idea that the falling phase of the fluorescence signal upon rinsing early (<170 s) after incubation with 3 μM Alexa-ATP can be used for quantification of catalytic activity of surface-adsorbed HMM molecules.

---

[3] This was calculated from the flow-cell volume (34 μL) and surface area (3.4 cm^2; see Materials and Methods) using a HMM surface density of 5400 μm^{-2}.

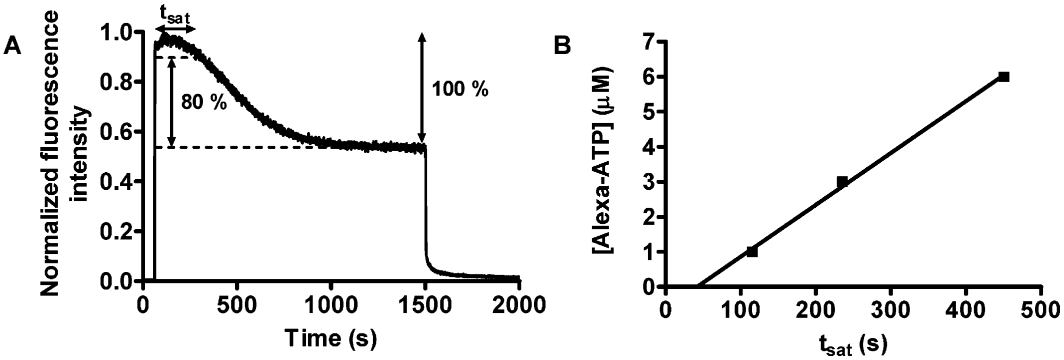

FIGURE 6: Method for obtaining the concentration of HMM active sites from TIRF data. (A) Experimental data for 6 μM Alexa-ATP in Figure 5C. The time interval, t_{sat}, is defined as the time after injection of Alexa-ATP until a decay of the fluorescence signal to 80% of the maximum value. (B). Plots of Alexa-ATP concentration against measured values of t_{sat} for incubation with 1, 3, and 6 μM Alexa-ATP. The concentration of HMM in the TIRF flow cell is now obtained from the slope of the regression line in panel B (straight line, slope 0.0148 ± 0.0007, $r^2 = 0.998$) divided by the average k_{cat} value (see text).

The results in Figure 5D provide further evidence for this idea. Here the fall in fluorescence upon rinsing is compared for the situations in Figure 5C (i.e., after complete hydrolysis; denoted "Alexa-ADP conditions") with situations (cf. Figure 5B,E,F) where Alexa-ATP is removed early after the first addition of the analogue. Under the latter conditions (denoted "Alexa-ATP condition") only a small fraction of the added Alexa-ATP had been hydrolyzed at the time of rinsing. Accordingly, the active sites of HMM would be occupied almost solely with Alexa-ATP.

It can be seen in Figure 5D that for rinsing in the Alexa-ADP condition fast phases in the fluorescence decay (except those due to bulk effects) virtually disappeared compared to the situation for the Alexa-ATP condition. Fitting of triple exponential functions to the data (Table 2) confirmed this view.

Thus, the two fast components in the exponential fits were significantly reduced in amplitude for the Alexa-ADP condition compared to the Alexa-ATP condition whereas the slowest rate process was of about the same magnitude for all experimental conditions. It is of interest to note that the two Alexa-ATP infusions of 3 μM with rinsing at 15 and 90 s after addition of the analogue both gave relatively similar rate constants and relative amplitudes of the different exponential processes (Figure 5D and Table 2).

The experiment in Figure 5C,D was complicated by a very prolonged incubation of the surface with HMM and prolonged periods of illumination. During the experimental period of several hours we found a continuous decrease in the amount of adsorbed HMM (by TIRF spectroscopy with excitation at 295 nm; see legend of Figure 5). This contributed to changes in the maximum amplitude of the fluorescence signal with subsequent Alexa-ATP incubations. However, importantly the early phase of the signal for the prolonged incubation with 3 μM Alexa-ATP (Figure 5D) superimposed well with the signal for one of the brief incubations with 3 μM Alexa-ATP (data not shown). Moreover, the latter incubation occurred just before the prolonged incubation, suggesting that the two runs should be readily comparable. Additionally, the time course of the decaying phase upon rinsing did not change appreciably with duration of HMM adsorption to the surface for the prolonged incubations (Figure 5D and Table 2).

Table 3: Triple Exponential Fits to the Decaying Phase of Fluorescence in TIRF Experiments[a]

	temperature: 25 ± 0.5 °C	
	k_{cat} (s^{-1})	amplitude (%)
phase 1	0.052 ± 0.002 (*n* = 4)	49 ± 2 (*n* = 4)
phase 2	0.0084 ± 0.0005 (*n* = 4)	8.8 ± 0.2 (*n* = 4)
phase 3	0.00045 ± 0.00004 (*n* = 4)	1.6 ± 0.2 (*n* = 4)
overall process	0.044 ± 0.002 (*n* = 4)	59 ± 2 (*n* = 4)

[a] Data (mean ± SEM) from four experiments with four different batches each of HMM and TMCS. SEM obtained from variability between experiments.

By measuring the time for the fluorescence signal in Figure 5C to decay to a value where 80% of the HMM molecules were believed to be saturated with Alexa-ATP (t_{sat} in Figure 6A), we could estimate the concentration of myosin active sites in the flow cell. This was achieved by dividing the slope of the plot in Figure 6B (0.0148 ± 0.0007 μM s^{-1}) with a k_{cat} value obtained as a weighted average of the two fastest exponential processes (0.052 ± 0.001 s^{-1}; cf. Table 2; SEM obtained from error propagation analysis). Such calculations gave a value of 0.285 ± 0.02 μM for the flow-cell concentration of HMM active sites compared to expected values between 0.18 and 0.36 μM (see above).

By using the falling phase of TIRF fluorescence signals (cf. Figure 5F), we performed a series of experiments to obtain statistical information about single-turnover hydrolysis of Alexa-ATP (3−5 μM) by HMM that was adsorbed to TMCS surfaces. Four separate experiments were performed at 25 ± 0.5 °C using four different batches of HMM and four different batches of TMCS-derivatized SiO_2 surfaces. A maximum of two brief incubations with Alexa-ATP was used in each experiment to minimize the effect of any time dependence of the results. Importantly, there was no significant difference in rate constants obtained in the exponential fits for the first and second run of each individual experiment (data not shown). The statistical analysis confirmed the results of Figure 5F. Thus, nonlinear regression analysis suggested that the exponential component with the fastest rate dominated in the fluorescence decay, corresponding to approximately 80% of the total single-turnover hydrolysis signal (25 °C; Table 3). The remaining two phases exhibited significantly lower rates and amplitudes than the first phase.

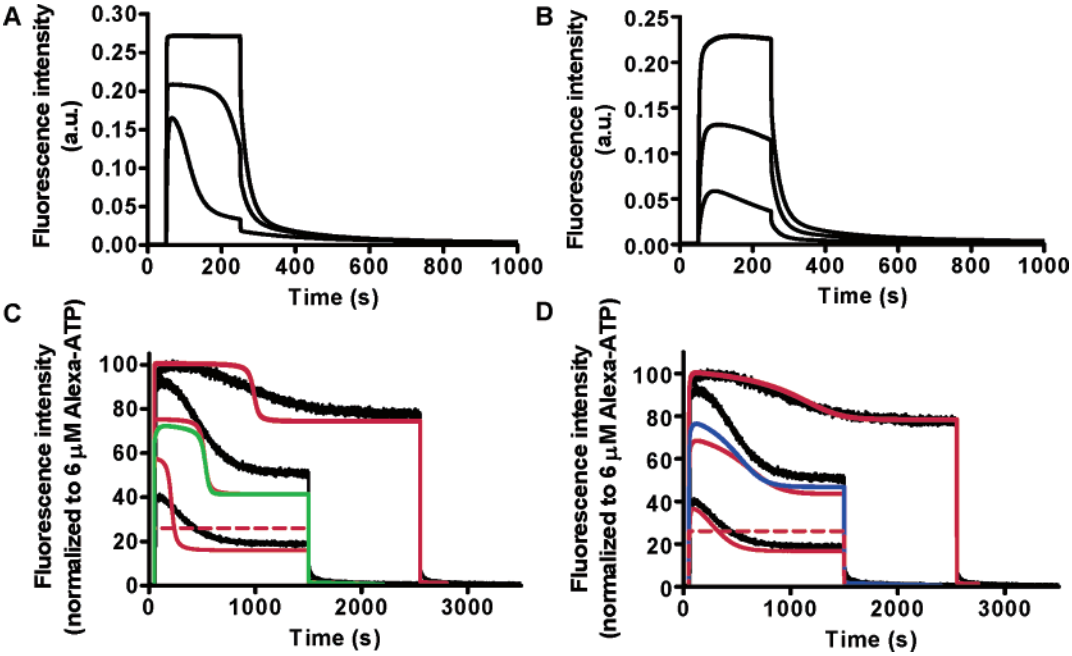

FIGURE 7: Simulated TIRF spectroscopy results based on the model in the Appendix (Scheme 3; see Supporting Information for details). (A) Model simulations of TIRF transients in response to short incubations with Alexa-ATP at 0.3 μM (lower trace), 1 μM (middle trace), and 3 μM (upper trace). Rate constants and equilibrium constants are as in Table 4 but $K_1k_2 = K_1k_2^s = 2\ \mu\text{M}^{-1}\ \text{s}^{-1}$. The HMM density was assumed to be 5400 μm^{-2} on the TMCS-derivatized TIRF slide and 2400 μm^{-2} on the stainless steel roof of the TIRF cell. On TMCS 81%, 16%, and 3% of the HMM molecules were assumed to be in the M, M^s, and M^{ss} configurations, respectively (see Scheme 3). (B) Simulations as in (A) but $K_1k_2 = 0.1\ \mu\text{M}^{-1}\ \text{s}^{-1}$ and $K_1k_2^s = 0.01\ \mu\text{M}^{-1}\ \text{s}^{-1}$. (C) Simulation of prolonged TIRF transients (colored lines) at 1, 3, and 6 μM Alexa-ATP superimposed on the experimental data from Figure 5C (black lines). Same parameter values as in (A) but $k_4 = 0.065\ \text{s}^{-1}$ and $k_4^s = 0.014\ \text{s}^{-1}$ (as measured for the given experiment; Table 3). Additionally, the green line represents a simulation of the fluorescence trace for 3 μM Alexa-ATP with $K_1k_2^s = 0.01\ \mu\text{M}^{-1}\ \text{s}^{-1}$. The dashed line represents the simulated bulk value for 3 μM Alexa-ATP. (D) Simulation of TIRF transients with the same parameter values as in (C) but with $K_1k_2 = 0.1\ \mu\text{M}^{-1}\ \text{s}^{-1}$ and $K_1k_2^s = 0.01\ \mu\text{M}^{-1}\ \text{s}^{-1}$. The blue line was obtained with the same parameter values, but the total HMM density was assumed to be 20% higher.

Due to a low signal-to-noise ratio, when monitoring changes in the tryptophan fluorescence upon ATP binding to the HMM, it was not possible to study the single turnover of ATP in the TIRF setup. However, by studying the steady-state hydrolysis of ATP and Alexa-ATP in regular TMCS flow cells and performing HPLC analysis, in combination with HMM depletion studies, it was possible to compare the overall hydrolysis rates of regular and fluorescent ATP. In contrast to results obtained in solution, hydrolysis was faster for ATP than Alexa-ATP when HMM was adsorbed to TMCS. Thus, this steady-state hydrolysis study yielded a k_{obs}^{SS} (see above) of 0.060 ± 0.0011 s^{-1} for ATP ($n = 2$) compared to a value of 0.051 ± 0.0016 s^{-1} ($n = 2$) for Alexa-ATP. It is interesting to note that this latter estimate of k_{cat} was slightly lower than the value given by the fast exponential process in the TIRF experiments (0.057 s^{-1} for the HMM preparation considered). This is similar to the situation in the solution studies where $k_{obs}^{SS} < k_{obs}$.

For ATP it is interesting to note that the hydrolysis rate on the surface was more than 2 times the value measured in solution for the same HMM preparation. In the case of the solution data both fluorescence spectroscopy ($k_{obs}^{SS} = 0.024$ s^{-1} and $k_{obs} = 0.026\ \text{s}^{-1}$) and HPLC-based determination (0.022 s^{-1}) of changes in ATP and ADP concentrations during hydrolysis gave similar results.

Computer Simulations of TIRF Results. The main features of the experimental data in Figure 5 can be reproduced by a model (Scheme 3 and Supporting Information) assuming three different HMM configurations on the TMCS surface. The decay phase of the fluorescence transient after rinsing was straightforward to reproduce in the simulations if one of the HMM configurations (representing 80% of all surface-adsorbed HMM molecules) is assumed to exhibit the same P_i release rate as in solution. Additionally, one has to postulate that one HMM configuration (approximately 15% of all molecules) exhibits about 10-fold slower P_i release than in solution. Finally, one configuration (a few percent of all molecules) must be assumed to bind Alexa-nucleotide with very slow off-kinetics. It was less straightforward to account for the varying shape of the transients after different amounts of added Alexa-ATP and different incubation times. In attempts to achieve this, we had to assume (Supporting Information) (1) slower binding of Alexa-ATP and Alexa-ADP to HMM than in solution and (2) binding rate constants for Alexa-ATP faster than the P_i release rates (or nucleotide off-rates) for each of the HMM configurations. The need to assume lower binding constants for Alexa-ATP than in solution is clearly illustrated by the simulations in Figure 7. Thus, the data in Figure 7A were obtained with $K_1k_2 = 2$ $\mu\text{M}^{-1}\ \text{s}^{-1}$ and $K_1k_2^s = 2\ \mu\text{M}^{-1}\ \text{s}^{-1}$ (same values as for K_1k_2 in solution) but with other parameter values given in Table 4. It is clear that the shape of the experimental fluorescence transients (e.g., those in Figure 5B) is poorly reproduced. This also applies to the situation with prolonged Alexa-ATP incubations as illustrated in Figure 7C. Here, the simulated data with $K_1k_2 = K_1k_2^s = 2\ \mu\text{M}^{-1}\ \text{s}^{-1}$ are superimposed on the experimental data of Figure 5C, and the considerable difference in shape of the experimental and simulated fluorescence signals is apparent. On the other hand, good reproduction of the experimental data is obtained with K_1k_2

Table 4: Kinetic Constants for ATP Hydrolysis by Myosin Used To Simulate the Alexa-ATP Fluorescence Transients in Solution (Scheme 1) and in the TIRF Setup (Scheme 3)

	optimal numerical values	
rate/equilibrium constant	for simulation in solution[a]	for simulation in TIRF setup[b]
K_1k_2 (μM^{-1} s^{-1})	2	0.1
K_3	10	10
k_4 (s^{-1})	0.05	0.05
k_5 (s^{-1})	3.5	3.5
k_{-5} (μM^{-1} s^{-1})	2	0.5
$K_1k_2{}^s$ (μM^{-1} s^{-1})	NA[c]	0.01
$K_3{}^s$	NA	10
$k_4{}^s$ (s^{-1})	NA	0.008
$k_5{}^s$ (s^{-1})	NA	3.5
$k_{-5}{}^s$ (μM^{-1} s^{-1})	NA	0.5
k_s (s^{-1})	NA	0.01
k_{-s} (s^{-1})	NA	0.001

[a] Numerical values obtained in the experiments of Figure 2 except K_3 from ref *3*. [b] Numerical values of K_1k_2, $K_1k_2{}^s$, k_4, $k_4{}^s$, k_{-5}, $k_{-5}{}^s$, k_s, and k_{-s} estimated to be consistent with Alexa-ATP transients in TIRF spectroscopy setup (Tables 2 and 3 and Supporting Information). Numerical values of K_3 from ref *3*. The rate constant k_5 assumed to be similar to the value in solution. The assumptions were made that $K_3 = K_3{}^s$, $k_5 = k_5{}^s$, and $k_{-5} = k_{-5}{}^s$. [c]NA = not applicable.

$= 0.1$ μM^{-1} s^{-1} and $K_1k_2{}^s = 0.01$ μM^{-1} s^{-1} (Figure 7B,D) and other parameter values given in Table 4. The fit is judged as good, considering the complexity of the experimental situation when it comes to other phases of the fluorescence transient than the multiexponential decay after rinsing (see Supporting Information).

One may consider the possibility that the experimental data in Figure 5 could be fitted with $K_1k_2 = 2$ μM^{-1} s^{-1}, as in solution, but with $K_1k_2{}^s = 0.01$ μM^{-1} s^{-1}, i.e., with a low value only for $K_1k_2{}^s$. However, as exemplified by the green trace in Figure 7C, this was clearly not the case.

Thus, in order to fit other features of the fluorescence transients than the multiexponential decay phase, it was necessary to assume that K_1k_2 was lower than in solution and, as further suggested by data in the Supporting Information, that $K_1k_2{}^s$ was lower than K_1k_2. In Figure 7D, the relative amplitude of the simulated TIRF signal for 3 μM Alexa-ATP was lower than the corresponding experimental trace when compared to the amplitudes for 1 and 6 μM Alexa-ATP. As illustrated by the blue line in Figure 7D, this may be partly accounted for by assuming a higher total HMM surface density (by about 20%) for the incubation with 3 μM Alexa-ATP. Since the experiment with 3 μM Alexa-ATP was performed first in the series, this modification in the simulations was consistent with a decay with time of the HMM density on the surfaces during the very prolonged experiment in Figure 5C. However, as can be seen in Figure 7D, the effect cannot fully explain the differences between experimental and simulated records. This suggests that there may be more complexities not taken into account in the simulations (e.g., decrease in Alexa-ATP binding of the remaining HMM molecules on the surface).

DISCUSSION

Alexa-ATP Fluorescence in the Presence of HMM. The quenching of Alexa-ATP fluorescence upon binding to HMM is similar to that observed for the 2′(3′)-ribose-derivatized analogue, fluorescein-EDA-ATP (FEDA-ATP) (*35*). The quenching of the FEDA-ATP fluorescence was associated with a quench also in tryptophan fluorescence and an increase in anisotropy. These observations lead to the proposal (*35*) that the effect may be attributed to stacking of the fluorophore with surface aromatic residues on the protein. Since also the quenching of Alexa-ATP was associated with a significant quench of the tryptophan fluorescence, a similar mechanism may be present in this case. We found that this effect was associated with energy transfer to Alexa-ATP, but there may also be a mechanism of quenching similar to that previously considered for FEDA-ATP. After complete hydrolysis of Alexa-ATP the fluorescence intensity was still lower than in the absence of HMM, suggesting that also Alexa-ADP exhibited lower emission when bound to HMM. However, the fluorescence emission of free Alexa-ATP and Alexa-ADP appeared to be similar. Thus, addition of 0.25 mM ATP, to displace the Alexa-ADP from the active site, brought the fluorescence intensity back to the value before addition of HMM.

The 20−30% quenching of the Alexa-ATP fluorescence upon binding to HMM would not be expected to pose a problem for observing the fluorophore in single molecule fluorescence experiments. The most commonly used analogue for such studies (*18*, *30*, *34*) has, so far, been Cy3-EDA-ATP, and at least one isomer of Cy3-EDA-ATP exhibited increased fluorescence intensity upon binding to HMM (*34*). However, considering the higher extinction coefficient (ϵ) and quantum yield (QY) of free Alexa-ATP (*54*) ($\epsilon = 250000$ cm^{-1} M^{-1}; QY ≈ 0.39) than of Cy3-ATP ($\epsilon = 150000$ cm^{-1} M^{-1}; QY $= 0.04$) (*36*, *53*, *54*), the quenching of Alexa-ATP fluorescence would be of minor concern. Additionally, as supported by our results, Alexa-ATP exhibits slow photobleaching (*54*). However, before use in single molecule fluorescence studies it will be important to evaluate other properties in some detail such as signal to background ratio in the TIRF microscope and the blinking properties of individual Alexa-ATP molecules. The latter evaluation will be important, e.g., in order to ensure that there is no slow blinking that can be confused with turnover (cf. discussion in refs *31* and *55*).

Catalytic Activity of HMM in Solution: Hydrolysis of ATP vs Different Isomers of Alexa-ATP. Four different Alexa-ATP isomers were detected in HPLC-based separation. As further argued below and in some detail in the Supporting Information, all of these isomers were hydrolyzed at similar rates by HMM.

Whereas the molecular structure of Alexa-ATP is currently proprietary information, the structure of Alexa-647 has been reported (*56*). This structure is shown in Figure 8 together with the most likely attachment point (U.S. Patents US2003064794 and US2004166515) for the *N*-(2-aminoethyl)urethane linker from the 2′ or 3′ positions on the ribose moiety of ATP. On the basis of this structural information we expect that the four observed isomers arise from the expected isomers (*28*) with the fluorophore attached to either the 2′- or 3′-hydroxyl group (which both are chiral centers) of the ribose moiety of ATP. For each of these isomers it is reasonable to believe that there exist two isomers with the linker attached to either the *R*- or *S*-conformation in the Alexa-647 moiety (chiral center indicated in the Alexa-647 structure in Figure 8). This is consistent with the findings that diastereomer isomers are possible to separate using a

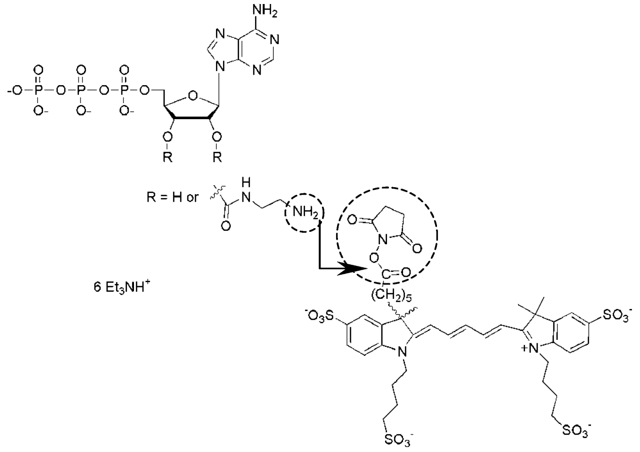

FIGURE 8: Proposed attachment of ATP via a linker to Alexa-647. R in the structure represents a linker between ATP and Alexa-647 [*O*-(*N*-(2-aminoethyl)urethane)] or hydrogen and shows that both of these structures can be attached to the 2′ or 3′ positions on the ribose moiety of ATP. Reactive groups in the linker (amine) and Alexa-647 (succinimidyl ester) are encircled, and the arrow in the image indicates the proposed attachment point for ATP to Alexa-647 via an amide bond.

C_{18} column as in our HPLC system (*57*, *58*). The HMM-catalyzed hydrolysis rates for different Alexa-ATP isomers differed only slightly and were quite similar (slightly higher) than that for ATP as observed for other ribose-modified ATP analogues (*34*−*36*). The difference in ATP hydrolysis rates between different isomers was lower than for the Cy3-EDA-ATP isomer studied previously (*36*) but similar to that observed for FEDA-ATP (*35*).

The similarity of the hydrolysis rates for all isomers was supported by fluorescence spectroscopy studies (for details see Supporting Information). Thus, like the decay in tryptophan fluorescence for ATP the increase in fluorescence of Alexa-ATP subsequent to steady-state hydrolysis was well fitted by a single exponential function. Particularly, we did not observe any slow components, similar to those observed with HMM adsorbed to the TMCS surface. The fluorescence spectroscopy data were consistent with the HPLC data in that hydrolysis of the Alexa-ATP was faster than hydrolysis of ATP.

The rates of individual steps in the HMM-catalyzed hydrolysis cycle for Alexa-ATP were further characterized using stopped-flow experiments. The magnitude of the second-order rate constant of Alexa-ATP binding to HMM was 2 $\mu M^{-1}\ s^{-1}$, similar to that previously reported for ATP (*20*). Thus, Alexa-ATP would exhibit a K_M value for myosin ($K_M = k_{cat}/K_1k_2$; e.g., ref *34*) lower than 0.1 μM. This is also consistent with the flat fluorescence trace during steady-state hydrolysis in Figure 2B. Results from a second series of stopped-flow experiments strongly support the view that P_i release is the rate-limiting step for the steady-state hydrolysis as it is for ATP. Thus, the fluorescence signal completely recovered with a half-time of 0.4 s to the prehydrolysis value after displacement of Alexa-ADP by ATP. Detailed analysis of the stopped-flow trace suggests that the recovery followed a double exponential time course with rate constants of about 6 and 1 s^{-1} for the fast and slow process, respectively. Both of these processes had similar amplitudes, and one may hypothesize that they are due, e.g., to different Alexa-ADP isomers. Importantly, however, both rate constants are considerably higher than the k_{cat} value for the turnover of Alexa-ATP by HMM and also considerably higher than any signals observed in the decaying phase of the TIRF signals in Figure 5.

The only rate constant in Scheme 1 that we did not probe in any detail is k_{-5}. The data in Figure 2A,B suggest that this constant was 2 $\mu M^{-1}\ s^{-1}$, about 4 times higher than that (0.5 $\mu M^{-1}\ s^{-1}$) reported previously. This value was obtained from the fluorescence intensities when only Alexa-ATP (during time period t_{ss} in Figure 2B) or only Alexa-ADP (before arrow II in Figure 2A) was bound to the active sites of HMM. However, an alternative interpretation that would be consistent with k_{-5} being equal to 0.5 $\mu M^{-1}\ s^{-1}$ would be that the quench of the Alexa-ADP upon binding to the active site was about twice as high as for Alexa-ATP. Importantly, whereas we could not fully distinguish between the alternative interpretations, this does not affect any of the main conclusions of the paper (e.g., as stated in the abstract).

In Vitro Motility Assay: ATP vs Alexa-ATP. The in vitro motility assay results show that Alexa-ATP is suitable as a substrate, not only for myosin but also for actomyosin. However, Alexa-ATP gave a lower V_{max} and a slightly higher K_M value than ATP for the sliding velocity. The reduction in V_{max} is in qualitative agreement with previous results for two other ribose-modified ATP analogues. Thus both Cy3-EDA-ATP and Cy5-EDA-ATP induced unloaded shortening velocity in skinned fibers about 2-fold more slowly than with ATP (*34*). There are a range of possibilities to explain the changes in V_{max} and K_M (cf. ref *48*). Competitive inhibition by certain Alexa-ATP isomers of myosin head detachment from actin could explain the higher K_M. This is possible in spite of the similar k_{cat} values since k_{cat} and V_{max} are limited by different steps in hydrolysis of ATP. Other possibilities to account for the reduction in V_{max} could be a reduced rate of release of Alexa-ADP from actomyosin or increased frictional resistance between actin filaments and the myosin heads with Alexa-nucleotide. With regard to the possibility of a reduced rate of Alexa-ADP release, this cannot be excluded on basis of previous studies using skinned muscle cells (*38*, *40*, *41*). In these studies changes in anisotropy were followed upon displacement of Alexa-ADP from the active site of the myosin cross-bridges, suggesting a half-time of about 5 ms. This is slightly slower than the rate of release expected for ADP under unloaded conditions (∼1000 s^{-1}) (*20*) but considerably faster than the release rate under isometric conditions (10−15 s^{-1}) (*59*). Thus, a direct comparison with the rate of release of ADP is difficult since the transition depends on cross-bridge strain.

It is important to note that, whereas we were unable to observe sliding filaments at Alexa-ATP concentrations greater than 1 mM, this is still considerable progress compared to a previous study of Cy5-EDA-ATP (*34*). In that study in vitro motility could not be observed at higher analogue concentrations than about 1 μM. Since Cy5-EDA-ATP and Alexa-ATP have similar excitation−emission spectra, the improvement in the present study is attributed to the use of Alexa-488-labeled actin filaments (instead of TRITC-labeled filaments). It is important to note, in this connection, that the motility quality (sliding velocity and fraction of motile filaments) has been shown to be similar for filaments labeled with TRITC-phalloidin and Alexa-488 phalloidin (*37*).

TIRF Spectroscopy Studies and Different HMM Configurations on TMCS Surfaces. In consistency with the present observations, we have in several recent studies (*22*−*24*, *43*) shown that HMM-propelled actin filament motility is of similar quality (velocity and fraction of motile filaments) on trimethylchlorosilane- (TMCS-) derivatized surfaces as on nitrocellulose. Of particular importance is the fact that the motility quality on TMCS has appeared to be more reproducible than on nitrocellulose and on several other silanes (*43*). This is consistent with the idea that properly derivatized TMCS surfaces exhibit a simple chemistry with a flat monolayer of trimethylsilyl groups (*43*). The properties of nitrocellulose surfaces are less well defined (*43*, *60*, *61*).

In view of these advantages of TMCS surfaces we have here used Alexa-ATP and TIRF spectroscopy to further characterize the function of the adsorbed HMM molecules. In these experiments changes in fluorescence intensity can be interpreted in terms of binding and hydrolysis of Alexa-ATP by HMM (see below). In principle, similar studies should also be possible to perform by following changes in tryptophan fluorescence upon hydrolysis of ATP. However, the tryptophan signal in the TIRF spectroscopy setup was too noisy for this type of study (unpublished observations).

The fluorescence signal observed upon addition of Alexa-ATP to a flow cell may be interpreted as follows. First, there is an immediate increase in Alexa-ATP emission due to bulk contribution and nonspecific binding of Alexa-ATP to HMM. This phase, synchronous with the increase of Alexa-ATP concentration in the TIRF cell, is followed by a complex phase with some variation in rate between experiments. This phase was slower than expected from the value of the binding rate constant K_1k_2 in solution (2 μM^{-1} s^{-1}). Whereas there was some variability in the rising phase, simulations suggest that slow binding of Alexa-ATP to HMM on the surfaces has to be postulated to account also for other aspects of the fluorescence transients, e.g., at low Alexa-ATP concentration (see Figure 7 and Supporting Information).

Upon rinsing with Alexa-ATP-free solution, within 15−170 s after addition of 3 μM Alexa-ATP to a TIRF cell with HMM, the fluorescence intensity first decayed in a rapid phase synchronous with the removal of Alexa-ATP. This rapid phase, attributed to bulk effects and nonspecific binding, was followed by a multiexponential decay toward the baseline. The latter multiexponential phase was not observed if a high concentration of ATP was infused to block binding of Alexa-ATP to the active sites of HMM. The obvious interpretation of the multiexponential nature of the decay process is therefore that it is due to the Alexa-nucleotide binding to the active sites of different HMM configurations on the surface. A simplified model, with three different HMM configurations, can simulate the most important features of the data. Comparison with the effect of rinsing after prolonged incubation and complete hydrolysis of Alexa-ATP (Figure 5C,D) suggests that there is one configuration (less than 4% of all HMM molecules) that strongly binds both Alexa-ATP and Alexa-ADP. The presence of this configuration was indicated by the very slowly decaying exponential process (rate constant $< \sim 0.001$ s^{-1}). This latter process was observed both after very brief (indicating fast binding kinetics) and prolonged exposures to 3 μM Alexa-ATP. Under the latter conditions all Alexa-ATP was consumed, leaving only Alexa-ADP to bind to the active site of HMM.

In addition to the very slow exponential process there were two faster exponential processes. The latter exhibited very small amplitudes if rinsing was delayed until after Alexa-ATP had been converted into Alexa-ADP. The small remaining fractions of the fast phases under these conditions are most likely attributed to the dissociation of Alexa-ADP. On the other hand, the two fast phases in the multiexponential decay dominated after short Alexa-ATP incubations. They could be simulated by the presence of two HMM configurations with k_{cat} for ATP hydrolysis of ~ 0.05 and ~ 0.008 s^{-1}, respectively. The amplitudes of these exponential phases corresponded to 83% and 15%, respectively, of fluorescence decay that was not attributed to bulk effects and nonspecific binding of Alexa-ATP (cf. Table 3).

In reality there probably exists a spectrum of myosin head configurations rather than just three. Thus, a stripping procedure using semilogarithmic plots of the data indicated the presence of at least four exponential processes. However, the decay of the fluorescence signal upon rinsing was well approximated by three exponential processes. The model with three different HMM configurations could account for the central aspects of the experimental data. However, due to the simplifications, e.g., neglecting the possibility of a spectrum of HMM configurations, the model simulations could not account for all details of the experimental traces. Accordingly, no attempts were made to quantify the fit of the model responses.

The existence of different myosin head configurations on the surface is consistent with proteolysis studies showing different HMM configurations on nitrocellulose (*25*). The idea of different myosin head configurations with different catalytic and actin-propelling capabilities is also in accordance with a previous model to account for the difference between motility on TMCS and SiO_2 (*23*). In terms of this model it was presumed that some adsorbed HMM molecules have low actin binding capability and, possibly, low ATPase activity. On experimental and different theoretical grounds it was proposed that these HMM molecules (termed HMM^N) have their heads tethered to the surface. The actin-propelling HMM molecules (termed HMM^C), on the other hand, were proposed to attach to the surface only via the C-terminal part of the S2 domain. It seems reasonable to presume that the proximity to the surface of the catalytic site of the HMM^N molecules accounts for the low k_{cat} values observed for a fraction of the myosin heads (corresponding to the slow exponential processes). Whether the slow kinetics is due to simple steric hindrance or minor structural changes in the HMM^N heads is not revealed by the current data. One possibility to account for a slow on-rate of Alexa-ATP for a fraction of the HMM molecules in the TIRF experiments may be slow diffusion of the large Alexa-ATP molecule to reach the active sites of the myosin heads. Under the current experimental conditions (incubation with HMM at 120 μg/mL) one would expect almost a monolayer of HMM on the surface with small intermolecular spaces and restricted diffusion of Alexa-ATP (*23*).

The present data suggest that the fraction of myosin heads in the HMM^N configurations was rather low on TMCS (<20%). Moreover, this value is probably an overestimate since the contribution to fluorescence intensity of myosin heads close to the surface (HMM^N) is expected to be higher than the contribution of myosin heads further away. This is due both to a stronger evanescent wave excitation (*23*) and to an apparent increase in fluorophore brightness close to a dielectric interface (*62*). The apparently low fraction of myosin heads in the HMM^N configurations supports previous conclusions (*23*, *43*) that TMCS is an excellent substrate for HMM adsorption in the in vitro motility assay. The fast process in the multiexponential decay had a rate similar (slightly higher) to that of Alexa-ATP turnover in solution, suggesting that this process indeed represents the rate-limiting P_i release step. Although the rates of all exponential phases exhibited similar temperature dependence, the possibility exists that not only the slowest phase but also the second slowest phase represents reversible binding of Alexa-ATP without hydrolysis. However, it is important to note that the interpretation of the data in terms of different HMM configurations is not invalidated by this idea.

Conclusions and Perspectives. In accordance with previous findings (*40*) that the myofibrillar ATPase was similar for ATP and Alexa-ATP, the present results have shown that Alexa-ATP is a good substrate both for myosin and for actomyosin. Whereas the steady-state hydrolysis of Alexa-ATP by heavy meromyosin in solution was slightly faster than that for ATP, the HMM-induced actin sliding velocity was lower with Alexa-ATP at close to saturating nucleotide concentration. The four different isomers of Alexa-ATP appeared to behave similarly with respect to hydrolysis by HMM. This is an advantage compared to, e.g., Cy3-EDA-ATP (*36*). Another advantage is the possibility to observe Alexa-488-labeled actin filaments in the presence of high (millimolar) concentrations of Alexa-ATP. The similarity in properties to ATP suggests that Alexa-ATP may be useful as a commercially available and highly photostable alternative to Cy3-EDA and Cy5-EDA-labeled ATP in a range of biophysical/biochemical studies. Further elucidation of the minor differences between actomyosin function with ATP and Alexa-ATP may also contribute to the in-depth understanding of the energy transduction mechanism. Interestingly, the combination of a higher hydrolysis rate than for ATP (in solution in the absence of actin) and a lower sliding velocity at saturating nucleotide concentration is similar to what has previously been observed with at least one drug (*48*, *63*) and several point mutations in switch II and the SH1−SH2 helices in the myosin head (*64*, *65*).

The use of Alexa-ATP to characterize HMM binding to TMCS suggested that a vast majority of the myosin heads are catalytically active. Our results show that they hydrolyze Alexa-ATP, and particularly ATP, at a higher average rate than in solution. This is consistent with the high-quality actomyosin function on TMCS. However, the observation of higher ATPase activity on the surface than in solution deserves attention when estimating HMM surface density on the basis of ATPase measurements. It is therefore interesting in this connection that our results suggest a quick and well-controlled TIRF microscopy method that does not depend on the assumption of similar ATPase activity on surfaces and in solution. The average k_{cat} value for the adsorbed myosin motors may first be obtained from the decaying phase of the fluorescence transient upon rinsing as in the TIRF spectroscopy studies (Figure 5F). The density of active sites should then be obtainable (using the same flow cell) from the time it takes for the surface-adsorbed HMM to convert the Alexa-ATP to Alexa-ADP (Figure 6). The usefulness of this method is based on the reduced fluorescence intensity in evanescent wave excitation after hydrolysis to Alexa-ADP as demonstrated in Figures 5 and 6. In order to obtain the density of catalytically active myosin heads, rather than the total active site concentration in the flow cell, it is important that the two surfaces of the cell are both functionalized in the same way (e.g., with TMCS). This was not the case for our experiment using the TIRF flow cell where one surface was made of stainless steel. On the other hand, the method should be readily applicable using a TIRF microscope and the type of flow cells routinely used for in vitro motility assay studies.

ACKNOWLEDGMENT

Professor Sven Tågerud, Professor Roland Isaksson, Associate Professor Susanne Wikman, and Dr. Mikael Nilsson are acknowledged for fruitful discussions and valuable advice.

APPENDIX

The ATP hydrolysis by myosin may be modeled by the kinetic Scheme 1 (see introduction) with the values of the rate constants in solution given in Table 4.

In order to model the hydrolysis of Alexa-ATP by surface-adsorbed HMM, Scheme 1 needs to be extended, e.g., to include different populations of myosin heads with different kinetic properties and nonspecific binding of Alexa-ATP to the HMM-coated surface. To take these and other aspects into account, Scheme 1 was first simplified by assuming that the states M ATP and M ADP P_i are in rapid equilibrium, leading to Scheme 2. In this scheme, the state representing the equilibrium between M ATP and M ADP P_i is denoted by MADP P_i and the rate constant $k_p = K_3k_4/(K_3 + 1)$ (see Scheme 1 and Table 4).

Scheme 2

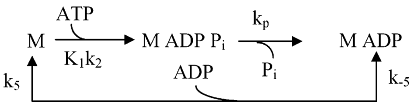

Now, the possibility of three different myosin configurations with different ATPase kinetics or only Alexa-nucleotide binding (without turnover) results in parallel kinetic schemes (Scheme 3). In this scheme, aATP and aADP denote Alexa-ATP and Alexa-ADP, respectively. The states M^{s}aADP P_i and M^{s}aADP represent the HMM configuration with slow

Scheme 3

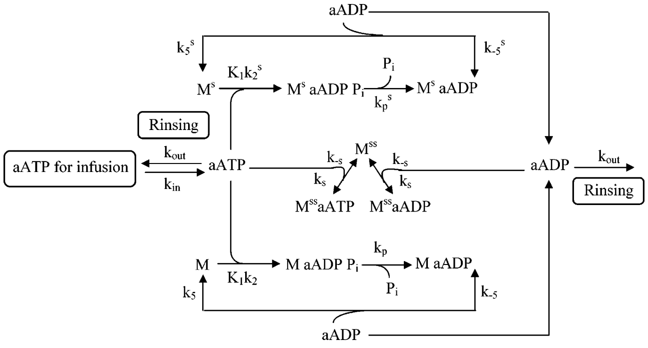

Alexa-ATP hydrolysis kinetics whereas the states represented by M^{ss}, M^{ss}aATP, and M^{ss}aADP represent HMM configurations that only bind Alexa-nucleotide without catalytic activity. This configuration was included in the simulation to account for the slowest phases of the multiexponential decay of the fluorescence transients in Figure 5. In addition to the HMM configurations adsorbed to the TMCS surface there were also catalytically active HMM molecules on the metal part of the TIRF cell (Figure 6). Whereas these were not probed by the evanescent wave excitation, they contributed to the overall conversion of Alexa-ATP to Alexa-ADP in the TIRF cell, thus indirectly affecting the TIRF signal. Therefore, this consumption of Alexa-ATP was taken into account assuming a rate suggested by the analysis in Figure 6. Another aspect that also was taken into account in the simulations is diffusion equilibration within the flow cell, e.g., upon large rapid binding of Alexa-ATP to surface-adsorbed HMM (for details see Supporting Information).

While taking the above complicating factors (e.g., HMM on metal and diffusion) into account, the system of ordinary differential equations governing Scheme 3 were solved numerically. Then a simulated fluorescence signal was obtained by setting

$$I = c_1[\text{aATP}] + c_2[\text{aADP}] + c_3[\text{MaATP}] + c_4[\text{MaADP}] + c_5[\text{M}^{\text{s}}\text{aATP}] + c_6[\text{M}^{\text{s}}\text{aADP}] + c_7[\text{M}^{\text{ss}}\text{aATP}] + c_8[\text{M}^{\text{ss}}\text{aADP}]$$

Here the square brackets ([ ]) represent concentrations of the different species in Scheme 3 whereas the coefficients c_1–c_8 represent the relative contribution to the fluorescence intensity of the different fluorescent species. These coefficients are determined both by the extinction coefficient and by the quantum yield of the fluorophores and also by the intensity of the evanescent wave excitation. The values for c_1 and c_2 were assumed to be identical ($c_1 = c_2$) and were calculated from the fluorescence intensity in the TIRF setup when the catalytic sites of all myosin heads were blocked by binding of regular ATP (5 mM ATP in the flow cell). The other constants apply to Alexa-ATP/Alexa-ADP species that are bound to the catalytic site of HMM molecules in different configurations. The values of these constants were all assumed to be identical and vary between $20c_1$ and $60c_1$ to obtain an appropriate relative value for the contribution from Alexa-ATP in the bulk/nonspecific binding.

Simulation of Experimental Data. A detailed description of the strategy for simulating experimental data is given in the Supporting Information. Numerical solution of the differential equations was achieved as described in Materials and Methods.

SUPPORTING INFORMATION AVAILABLE

(1) Derivatization of fused silica TIRF slides with trimethylchlorosilane (TMCS), (2) in vitro motility assays, (3) determination of quantum yield for Alexa-ATP, and (4) detailed description of incubation procedures during TIRF experiments; in addition, more details relating to HPLC-aided analysis of Alexa-ATP and Alexa-ADP during steady-state hydrolysis and more details about the temperature sensitivity of Alexa-ATP fluorescence and simulation of experimental data, including the Simnon source code for the solution of differential equations. This material is available free of charge via the Internet at http://pubs.acs.org.

REFERENCES

1. Huxley, A. F. (1957) Muscle structure and theories of contraction, *Prog. Biophys. Biophys. Chem. 7*, 255–318.
2. Huxley, H. E. (1969) The mechanism of muscular contraction, *Science 164*, 1356–1365.
3. Howard, J. (2001) *Mechanics of motor proteins and the cytoskeleton*, Sinauer Associates, Sunderland, MA.
4. Woledge, R. C., Curtin, N. A., and Homsher, E. (1985) *Energetic aspects of muscle contraction*, Academic Press, London.
5. Bagshaw, C. R., and Trentham, D. R. (1974) The characterization of myosin-product complexes and of product-release steps during the magnesium ion-dependent adenosine triphosphatase reaction, *Biochem. J. 141*, 331–349.
6. Harada, Y., Noguchi, A., Kishino, A., and Yanagida, T. (1987) Sliding movement of single actin filaments on one-headed myosin filaments, *Nature 326*, 805–808.
7. Kron, S. J., Toyoshima, Y. Y., Uyeda, T. Q., and Spudich, J. A. (1991) Assays for actin sliding movement over myosin-coated surfaces, *Methods Enzymol. 196*, 399–416.
8. Kron, S. J., and Spudich, J. A. (1986) Fluorescent actin-filaments move on myosin fixed to a glass-surface, *Proc. Natl. Acad Sci. U.S.A. 83*, 6272–6276.
9. Tsiavaliaris, G., Fujita-Becker, S., and Manstein, D. J. (2004) Molecular engineering of a backwards-moving myosin motor, *Nature 427*, 558–561.
10. Wells, A. L., Lin, A. W., Chen, L. Q., Safer, D., Cain, S. M., Hasson, T., Carragher, B. O., Milligan, R. A., and Sweeney, H. L. (1999) Myosin VI is an actin-based motor that moves backwards, *Nature 401*, 505–508.
11. Toyoshima, Y. Y., Kron, S. J., McNally, E. M., Niebling, K. R., Toyoshima, C., and Spudich, J. A. (1987) Myosin subfragment-1 is sufficient to move actin filaments in vitro, *Nature 328*, 536–539.
12. Harada, Y., Sakurada, K., Aoki, T., Thomas, D. D., and Yanagida, T. (1990) Mechanochemical coupling in actomyosin energy transduction studied by in vitro movement assay, *J. Mol. Biol. 216*, 49–68.
13. Uyeda, T. Q., Kron, S. J., and Spudich, J. A. (1990) Myosin step size. Estimation from slow sliding movement of actin over low densities of heavy meromyosin, *J. Mol. Biol. 214*, 699–710.
14. Finer, J. T., Simmons, R. M., and Spudich, J. A. (1994) Single myosin molecule mechanics: piconewton forces and nanometre steps, *Nature 368*, 113–139.
15. Veigel, C., Wang, F., Bartoo, M. L., Sellers, J. R., and Molloy, J. E. (2002) The gated gait of the processive molecular motor, myosin V, *Nat. Cell Biol. 4*, 59–65.
16. Tyska, M. J., Dupuis, D. E., Guilford, W. H., Patlak, J. B., Waller, G. S., Trybus, K. M., Warshaw, D. M., and Lowey, S. (1999) Two heads of myosin are better than one for generating force and motion, *Proc. Natl. Acad. Sci. U.S.A. 96*, 4402–4407.
17. Kitamura, K., Tokunaga, M., Iwane, A. H., and Yanagida, T. (1999) A single myosin head moves along an actin filament with regular steps of 5.3 nanometres, *Nature 397*, 129–134.
18. Ishijima, A., Kojima, H., Funatsu, T., Tokunaga, M., Higuchi, H., Tanaka, H., and Yanagida, T. (1998) Simultaneous observation of individual ATPase and mechanical events by a single myosin molecule during interaction with actin, *Cell 92*, 161–171.
19. Toyoshima, Y. Y., Kron, S. J., and Spudich, J. A. (1990) The myosin step size: measurement of the unit displacement per ATP hydrolyzed in an in vitro assay, *Proc. Natl. Acad. Sci. U.S.A. 87*, 7130–7134.
20. Nyitrai, M., Rossi, R., Adamek, N., Pellegrino, M. A., Bottinelli, R., and Geeves, M. A. (2006) What limits the velocity of fast-skeletal muscle contraction in mammals?, *J. Mol. Biol. 355*, 432–442.
21. Månsson, A., Nicholls, I. A., Omling, P., Tågerud, S., and Montelius, L. (2007) Nanotechnology enhanced functional assays of actomyosin motility—potentials and challenges, *Lect. Notes Phys. 711*, 385–406.
22. Bunk, R., Sundberg, M., Nicholls, I. A., Omling, P., Tågerud, S., Månsson, A., and Montelius, L. (2005) Guiding motor-propelled molecules with nanoscale precision through silanized bi-channel structures, *Nanotechnology 16*, 710–717.

23. Sundberg, M., Balaz, M., Bunk, R., Rosengren-Holmberg, J. P., Montelius, L., Nicholls, I. A., Omling, P., Tågerud, S., and Månsson, A. (2006) Selective spatial localization of actomyosin motor function by chemical surface patterning, *Langmuir 22*, 7302−7312.
24. Sundberg, M., Bunk, R., Albet-Torres, N., Kvennefors, A., Persson, F., Montelius, L., Nicholls, I. A., Ghatnekar-Nilsson, S., Omling, P., Tågerud, S., and Månsson, A. (2006) Actin filament guidance on a chip: Toward high-throughput assays and lab-on-a-chip applications, *Langmuir 22*, 7286−7295.
25. Toyoshima, Y. Y. (1993) How are myosin fragments bound to nitrocellulose film?, *Adv. Exp. Med. Biol. 332*, 259−265.
26. VanBuren, P., Palmiter, K. A., and Warshaw, D. M. (1999) Tropomyosin directly modulates actomyosin mechanical performance at the level of a single actin filament, *Proc. Natl. Acad. Sci. U.S.A. 96*, 12488−12493.
27. Guo, B., and Guilford, W. H. (2004) The tail of myosin reduces actin filament velocity in the in vitro motility assay, *Cell Motil. Cytoskeleton 59*, 264−272.
28. Bagshaw, C. (2001) ATP analogues at a glance, *J. Cell Sci. 114*, 459−460.
29. Funatsu, T., Harada, Y., Tokunaga, M., Saito, K., and Yanagida, T. (1995) Imaging of single fluorescent molecules and individual ATP turnovers by single myosin molecules in aqueous solution, *Nature 374*, 555−559.
30. Conibear, P. B., Kuhlman, P. A., and Bagshaw, C. R. (1998) Measurement of ATPase activities of myosin at the level of tracks and single molecules, *Adv. Exp. Med. Biol. 453*, 15−26 (discussion 26−27).
31. Brau, R. R., Tarsa, P. B., Ferrer, J. M., Lee, P., and Lang, M. J. (2006) Interlaced optical force-fluorescence measurements for single molecule biophysics, *Biophys. J. 91*, 1069−1077.
32. Webb, M. R., Reid, G. P., Munasinghe, V. R., and Corrie, J. E. (2004) A series of related nucleotide analogues that aids optimization of fluorescence signals in probing the mechanism of P-loop ATPases, such as actomyosin, *Biochemistry 43*, 14463−14471.
33. Tokunaga, M., Kitamura, K., Saito, K., Iwane, A. H., and Yanagida, T. (1997) Single molecule imaging of fluorophores and enzymatic reactions achieved by objective-type total internal reflection fluorescence microscopy, *Biochem. Biophys. Res. Commun. 235*, 47−53.
34. Oiwa, K., Eccleston, J. F., Anson, M., Kikumoto, M., Davis, C. T., Reid, G. P., Ferenczi, M. A., Corrie, J. E., Yamada, A., Nakayama, H., and Trentham, D. R. (2000) Comparative single-molecule and ensemble myosin enzymology: sulfoindocyanine ATP and ADP derivatives, *Biophys. J. 78*, 3048−3071.
35. Conibear, P. B., Jeffreys, D. S., Seehra, C. K., Eaton, R. J., and Bagshaw, C. R. (1996) Kinetic and spectroscopic characterization of fluorescent ribose-modified ATP analogs upon interaction with skeletal muscle myosin subfragment 1, *Biochemistry 35*, 2299−2308.
36. Oiwa, K., Jameson, D. M., Croney, J. C., Davis, C. T., Eccleston, J. F., and Anson, M. (2003) The 2′-O- and 3′-O-Cy3-EDA-ATP-(ADP) complexes with myosin subfragment-1 are spectroscopically distinct, *Biophys. J. 84*, 634−642.
37. Balaz, M., and Mansson, A. (2005) Detection of small differences in actomyosin function using actin labeled with different phalloidin conjugates, *Anal. Biochem. 338*, 224−236.
38. Borejdo, J., Shepard, A., Dumka, D., Akopova, I., Talent, J., Malka, A., and Burghardt, T. P. (2004) Changes in orientation of actin during contraction of muscle, *Biophys. J. 86*, 2308−2317.
39. Steigmiller, S., Zimmermann, B., Diez, M., Borsch, M., and Graber, P. (2004) Binding of single nucleotides to H$^+$-ATP synthases observed by fluorescence resonance energy transfer, *Bioelectrochemistry 63*, 79−85.
40. Shepard, A., and Borejdo, J. (2004) Correlation between mechanical and enzymatic events in contracting skeletal muscle fiber, *Biochemistry 43*, 2804−2811.
41. Shepard, A. A., Dumka, D., Akopova, I., Talent, J., and Borejdo, J. (2004) Simultaneous measurement of rotations of myosin, actin and ADP in a contracting skeletal muscle fiber, *J. Muscle Res. Cell Motil. 25*, 549−557.
42. Katayama, E. (1998) Quick-freeze deep-etch electron microscopy of the actin-heavy meromyosin complex during the in vitro motility assay, *J. Mol. Biol. 278*, 349−367.
43. Sundberg, M., Rosengren, J. P., Bunk, R., Lindahl, J., Nicholls, I. A., Tågerud, S., Omling, P., Montelius, L., and Månsson, A. (2003) Silanized surfaces for in vitro studies of actomyosin function and nanotechnology applications, *Anal. Biochem. 323*, 127−138.
44. Månsson, A., Sundberg, M., Bunk, R., Balaz, M., Nicholls, I. A., Omling, P., Tegenfeldt, J. O., Tågerud, S., and Montelius, L. (2005) Actin-based molecular motors for cargo transportation in nanotechnology—potentials and challenges, *IEEE Trans. Adv. Packag. 28*, 547−555.
45. Månsson, A., Sundberg, M., Balaz, M., Albet-Torres, N., Vikhorev, P., O'Mahony, J., Charlton, C., Kvennefors, A., Ghatnekar-Nilsson, S. G., Bunk, R., Tågerud, S., Nicholls, I. A., Omling, P., Heidari, B., and Montelius, L. (2006) Protein-surface interactions and nanotechnology assisted in vitro motility assyas, *J. Muscle Res. Cell Motil. 27*, 482.
46. Balaz, M., Sundberg, M., Bunk, R., Nicholls, I. A., Tågerud, S., Omling, P., Montelius, L., and Månsson, A. (2006) Towards nanotechnology assisted in vitro motility studies of actomyosin function—the importance of protein-surface interactions, Abstract of International Workshop on Single Molecule Analysis, Okinawa, Japan, 2006.
47. Sata, M., Sugiura, S., Yamashita, H., Momomura, S., and Serizawa, T. (1993) Dynamic interaction between cardiac myosin isoforms modifies velocity of actomyosin sliding in vitro, *Circ. Res. 73*, 696−704.
48. Klinth, J., Arner, A., and Månsson, A. (2003) Cardiotonic bipyridine amrinone slows myosin-induced actin filament sliding at saturating [MgATP], *J. Muscle Res. Cell Motil. 24*, 15−32.
49. Pardee, J. D., and Spudich, J. A. (1982) Purification of muscle actin, *Methods Cell Biol. 24*, 271−289.
50. Månsson, A., and Tågerud, S. (2003) Multivariate statistics in analysis of data from the in vitro motility assay, *Anal. Biochem. 314*, 281−293.
51. Samizo, K., Ishikawa, R., Nakamura, A., and Kohama, K. (2001) A highly sensitive method for measurement of myosin ATPase activity by reversed-phase high-performance liquid chromatography, *Anal. Biochem. 293*, 212−215.
52. Childs, K. F., Ning, X. H., and Bolling, S. F. (1996) Simultaneous detection of nucleotides, nucleosides and oxidative metabolites in myocardial biopsies, *J. Chromatogr., Sect. B: Biomed. Appl. 678*, 181−186.
53. Mujumdar, R. B., Ernst, L. A., Mujumdar, S. R., Lewis, C. J., and Waggoner, A. S. (1993) Cyanine dye labeling reagents—Sulfoindocyanine succinimidyl esters, *Bioconjugate Chem. 4*, 105−111.
54. Berlier, J. E., Rothe, A., Buller, G., Bradford, J., Gray, D. R., Filanoski, B. J., Telford, W. G., Yue, S., Liu, J. X., Cheung, C. Y., Chang, W., Hirsch, J. D., Beechem, J. M., Haugland, R. P., and Haugland, R. P. (2003) Quantitative comparison of long-wavelength Alexa Fluor dyes to Cy dyes: Fluorescence of the dyes and their bioconjugates, *J. Histochem. Cytochem. 51*, 1699−1712.
55. Rasnik, I., McKinney, S. A., and Ha, T. (2006) Nonblinking and long-lasting single-molecule fluorescence imaging, *Nat. Methods 3*, 891−893.
56. Chiuman, W., and Li, Y. F. (2007) Efficient signaling platforms built from a small catalytic DNA and doubly labeled fluorogenic substrates, *Nucleic Acids Res. 35*, 401−405.
57. Bergqvist, Y., Doverskog, M., and Alkabbani, J. (1994) High-performance liquid-chromatographic determination of (Sr)-enantiomers and (Rs)-enantiomers of mefloquine in plasma and capillary blood sampled on paper after derivatization with (−)-1-(9-fluorenyl)ethyl chloroformate, *J. Chromatogr., Sect. B: Biomed. Appl. 652*, 73−81.
58. Gutheil, W. G., and Bachovchin, W. W. (1993) Separation of L-Pro-DL-Boropro into its component diastereomers and kinetic-analysis of their inhibition of dipeptidyl peptidase. 4. A new method for the analysis of slow, tight-binding inhibition, *Biochemistry 32*, 8723−8731.
59. Dantzig, J. A., Hibberd, M. G., Trentham, D. R., and Goldman, Y. E. (1991) Cross-bridge kinetics in the presence of MgADP investigated by photolysis of caged ATP in rabbit psoas muscle fibres, *J. Physiol. 432*, 639−680.
60. Månsson, A., Klinth, J., Johansson-Karlsson, E., Widén, C., Johnsson, J., and Montelius, L. (2001) Scanning probe microscopy study of myosin binding, topography and elastic properties of thin nitrocellulose films, *Biophys. J. 80*, 77a.
61. Barbosa, I. V. M., Merquior, D. M., and Peixoto, F. C. (2005) Continuous modelling and kinetic parameter estimation for cellulose nitration, *Chem. Eng. Sci. 60*, 5406−5413.

62. Enderlein, J. (1999) Fluorescence detection of single molecules near a solution/glass interface—an electrodynamic analysis, *Chem. Phys. Lett. 308*, 263−266.

63. Bottinelli, R., Cappelli, V., Morner, S. E., and Reggiani, C. (1993) Effects of amrinone on shortening velocity and force development in skinned skeletal muscle fibres, *J. Muscle Res. Cell Motil. 14*, 110−120.

64. Suzuki, Y., Ohkura, R., Sugiura, S., Yasuda, R., Kinoshita, K., Jr., Tanokura, M., and Sutoh, K. (1997) Modulation of actin filament sliding by mutations of the SH2 cysteine in *Dictyostelium* myosin II, *Biochem. Biophys. Res. Commun. 234*, 701−706.

65. Sasaki, N., Shimada, T., and Sutoh, K. (1998) Mutational analysis of the switch II loop of *Dictyostelium* myosin II, *J. Biol. Chem. 273*, 20334−20340.

BI700211U